Biobased nucleation agents for poly-L-(lactic acid) – Effect on crystallization, rheological and mechanical properties

Mohamed Aouay[a], Albert Magnin[b], Jean-Luc Putaux[c], Sami Boufi[a,*]

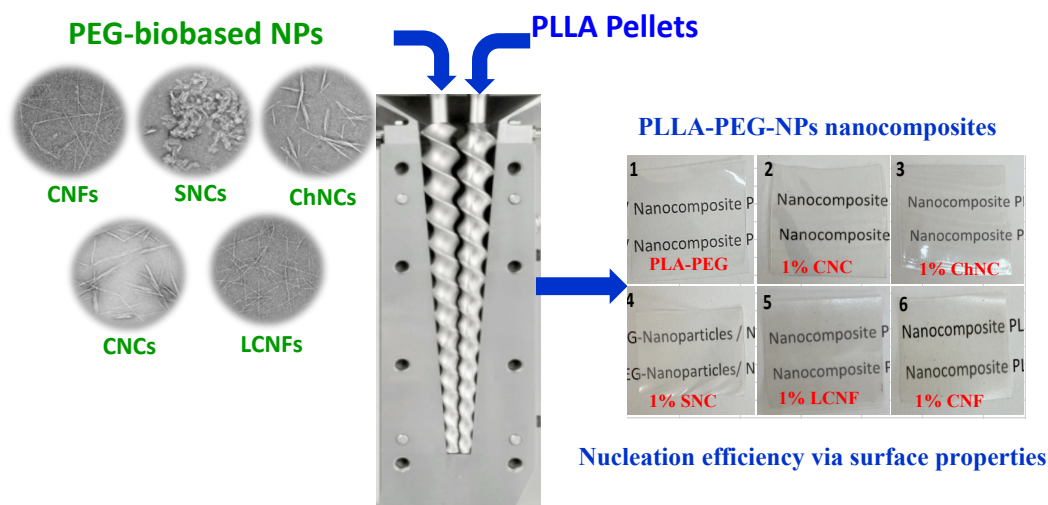[a] University of Sfax - LMSE - Faculty of Science - BP 802 - 3018 Sfax, Tunisia
[b] Univ. Grenoble Alpes, CNRS, Grenoble INP, LRP, F-38000 Grenoble, France
[c] Univ. Grenoble Alpes, CNRS, CERMAV, F-38000 Grenoble, France

* corresponding author: e-mail: sami.boufi@fss.rnu.tn

PEG-biobased NPs

PLLA Pellets

CNFs   SNCs   ChNCs

CNCs   LCNFs

PLLA-PEG-NPs nanocomposites
Before annealing

1	2	3
Nanocomposite P	Nanocomposite	Nanocomposite Pl
Nanocomposite P	Nanocomposite	Nanocomposite P
PLA-PEG	**1% CNC**	**1% ChNC**
4	5	6
G-Nanoparticles / N	Nanocomposite P	Nanocomposite PL
EG-Nanoparticles/ N	Nanocomposite F	Nanocomposite Pl
1% SNC	**1% LCNF**	**1% CNF**

Nucleation efficiency via surface properties

Abstract

In the present work, the nucleating aptitude for poly-L-(lactic acid) (PLLA) of several biobased nanoparticles (NPs) with different morphologies and surface properties, including cellulose nanofibrils with and without lignin (LCNFs and CNFs) as well as cellulose, chitin and starch nanocrystals (CNCs, ChNCs and SNCs), was investigated. A single melt-processing step using a small amount of poly(ethylene glycol) (PEG) as carrier for the NPs was adopted to prepare films with the same nanofiller content of 1 wt%. The nucleation efficiency was investigated by differential scanning calorimetry using Avrami's and Lauritzen–Hoffman's secondary nucleation theory. The crystallization half-time was found to change considerably according to the morphology and surface properties of the NPs, with the lowest time observed for CNFs and CNCs, followed by ChNCs, SNCs and LCNFs. Comparing the surface energy components of the different nucleating agents, it was found that the nanofiller with the highest γ^p had the lowest $t_{1/2}$ and demonstrated the most effective nucleating aptitude. The evolution of the melt rheological properties of the different compositions, and the mechanical and optical properties of the films with and without a short annealing treatment were also studied.

1. Introduction

Market demand for poly-L-(lactic acid) (PLLA) has steadily grown over the past decades, with a marked interest in packaging industry as a substitute to materials based on polypropylene (PP) and poly(ethylene terephthalate) (PET). The composability of PLLA and its biodegradability only under specific conditions in terms of temperature, humidity and soil composition, have prompted its potential use in durable structural materials and textiles [1]. However, although being crystallizable, PLLA-based products prepared by a conventional melt-processing route are almost fully amorphous, resulting in a poor heat resistance (heat distortion temperature HTD < 55 °C) and low barrier properties, that narrow its potential industrial applications where heat-resistance is required. Therefore, studies on improving the crystallization are crucial to widen the application of PLLA. Indeed, owing to a relatively low glass transition temperature (T_g), up to about 60 °C, the low degree of crystallinity of PLLA results in a material losing its thermomechanical stability once the temperature is approaching T_g. This restricts the widescale applications of PLLA in materials where dimensional stability is requested such as cutlery and drinking cups. Without an annealing treatment, the degree of crystallinity of PLLA does not exceed 10%, which is not enough to preserve the form-stability over 60 °C. The crystalline phase in PLLA would provide heat resistance and stiffness in trays, cups and plates, enhance the barrier and chemical resistance in films [2], and impart a higher strength to textile fibers.

The most popular approach to improve the crystallinity of a polymer is to add a nucleating agent that increases the rate of crystallization by reducing the free energy needed for the formation of stable nuclei with a critical size on which lamellar crystallites can grow. As a result, the temperature at which the polymer starts to crystallize from the melt is increased, as are the rate of nucleation and overall rate of crystallization. Numerous parameters are affecting the nucleating ability of the additive including, the size, morphology, their dispersion degree in the polymer matrix, the surface free energy, the roughness and the crystalline microstructure [3]. Nucleating agents also promote the formation of smaller and more numerous crystallites, which positively affects the optical properties, reducing haze and hence improving clarity.

More specifically, the use of nanoscale fillers as nucleating agents offering a large surface area would further enhance the crystallization at low contents. This strategy has been extensively explored in PLLA by testing a broad class of nucleating agents such as talc [4], N,N′-ethylene bis-stearamide (EBS) [5], carbon-based materials [6,7], amide and hydrazide compounds [8], calcium carbonate ($CaCO_3$) [9], nano-$CaCO_3$ [10], organic and cellulose fibers [11,12], montmorillonite [13] and silica [14].

Due to their biodegradability, lack of toxicity, safety to use and availability, biobased nanoparticles (NPs) from renewable resources such as cellulose nanofibrils (CNFs) as well as cellulose, chitin and starch nanocrystals (CNCs, ChNCs and SNCs, respectively) are emerging constituents whose morphology and surface properties may be beneficial for use as both nucleating and reinforcing agents in PLLA matrices.

CNCs have been the most studied biobased nucleating agent for PLLA [15-18]. For instance, using only 1 wt% of partially silylated CNCs, the crystallization rate strongly increased, whereas unmodified CNCs did not have such a marked effect [19]. CNCs with different surface properties were prepared using sulfuric, hydrochloric, phosphoric or nitric acid and were included in a lyophilized form in PLLA by melt extrusion at a content from 1 to 3 wt% [20]. In order to increase the compatibility of nanocellulose with PLLA and improve its dispersion, lignin-coated cellulose nanocrystals (LCNCs) were incorporated up to 2 wt% by direct melt-processing. They were shown to be an excellent nucleating agent for PLLA, helping to achieve optimum physical properties and hydrolytic stability [21]. Nanochitins, that include nanofibers (ChNFs) and nanocrystals (ChNCs), are other types of biobased NPs that are gaining popularity in nanocomposite applications. Although much less studied than CNCs or CNFs, the aptitude of ChNCs to act as nucleating agent for PLLA has been demonstrated [22].

However, while the colloidal stability of biobased NPs in water can be ensured by controlling their surface charge, these NPs tend to aggregate, often irreversibly, once the water is removed by drying without the addition of a water-soluble polymer capable of generating a physical barrier opposing the contacts between NPs. This aspect limits their use in the dry form, namely when the objective is to disperse the NPs within polymer matrices by a conventional melt-processing route. This inevitably results in a huge decrease in their efficiency as a nucleating agent. One simple approach is to use a plasticizer as carrier for the NPs to prevent their aggregation after drying, then mix the plasticizer-NP system with PLLA by conventional melt processing.

In the present work, PLLA films containing different biobased NPs were prepared by single melt processing using a small amount of poly(ethylene glycol) (PEG) as carrier to avoid the aggregation of the NPs. The main objective was to investigate the aptitude of biobased NPs with different morphologies and surface properties to act as nucleating agents and study the effect of the inclusion of a small amount of NPs (1 wt%) on the crystallization behavior, melt-rheology and mechanical properties of PLLA. Although numerous papers have demonstrated the capacity of biobased NPs to act as nucleating agents, comparing the nucleating efficiency of the different NPs was challenging, given the dissimilarity in their processing routes and the different methods adopted for investigating their nucleating efficiency.

2. Materials and Methods

2.1. Materials

A commercial PLLA from NaturePlast (PLE 005-France) was used as matrix for the nanocomposite films. PEG (molecular weight 35000 g mol^{-1}), purchased from Sigma Aldrich, was used as plasticizer. Never-dried eucalyptus pulp (NDEP) provided by Torraspapel (50 wt% water) and crab shell chitin from Sigma Aldrich were used for the production of CNFs and ChNCs respectively. CNCs were directly purchased from CelluForce. Sodium bromide (NaBr), 2,2,6,6-tetramethylpiperidine-1-oxyl radical (TEMPO) and hydrochloric acid (HCl) were purchased from Sigma Aldrich. Sodium hypochlorite (NaClO) was a standard commercial product with ClO$^-$ concentration around 2.8%.

2.2. Preparation of nanoparticles

CNFs, ChNCs and SNCs were prepared according to our previous works [23,24]. CNFs were prepared by high-pressure homogenization (HPH – 5 passes at 600 bar) of TEMPO-mediated oxidized bleached eucalyptus fibers with a carboxyl content around 1400 µmol g^{-1}. LCNFs were prepared by HPH of TEMPO-mediated oxidized date palm fibers with a carboxyl content around 600 µmol g^{-1}. Since the initial fibers had not been bleached, the residual lignin content of the LCNFs was around 15 wt%, and the hemicellulose and cellulose contents around 22 and 56 wt%, respectively. Details on HPH disintegration were given in our previous work [25].

2.3. Transmission electron microscopy (TEM) of nanoparticles

Droplets of different nanoparticle aqueous suspensions (*ca.* 0.001 wt%) were deposited onto carbon-coated copper grids that have been glow-discharged. A drop of uranyl acetate negative stain (2 wt%) was applied to the specimens before drying. The excess stain was wiped with filter paper, and the remaining liquid film was allowed to dry. The specimens were observed with a JEOL JEM 2100-Plus microscope operating at a 200-kV voltage and the images were recorded with a Gatan Rio 16 digital camera. The particle dimensions were determined from the TEM images using the ImageJ software.

2.4. PLLA-PEG-NPs composite processing

Suspensions of the different NPs with PEG were prepared in order to produce NP-PEG blends. In brief, aqueous NP suspensions (corresponding to 1 g dry NPs) with a solid content around 1 wt% were first sonicated for 1 min at a 70% amplitude (Sonics Vibracel Model CV33) to ensure an effective dispersion, and mixed with 5 g PEG. After a 1-h stirring, the mixture was poured into a glass Petri dish, dried for 24 h at 40 °C, and milled manually into pellets. The PLLA and NP-PEG pellets were fed together in a twin-screw DSM-Xplore15cc Microcompounder and extruded at

190 °C and 100 rpm for 5 min. The composite was then retrieved as a thin film using a flat sheet die with a 3×0.15 mm^2 rectangular cross-section. **Table 1** summarizes the formulation of prepared materials. Neat PLLA was used as a control while plasticized and reinforced PLLA samples were used to investigate the effects of NPs on the film crystallinity.

Table 1. Composition of prepared materials (wt%).

Sample	PLLA	PEG	NPs
Neat PLLA	100	0	0
PLLA-PEG	95	5	0
PLLA-PEG-NPs	94	5	1

2.5. Differential scanning calorimetry (DSC)

DSC thermograms were recorded under nitrogen atmosphere using a Perkin-Elmer differential scanning calorimeter. Approximately 8 mg of each sample was hermetically packed in an aluminum pan. For the non-isothermal crystallization, the samples were heated from 25 to 200 °C and then cooled to 25 °C and reheated to 200 °C. The same heating/cooling rate of 10 °C min^{-1} was adopted for all cycles.

Isothermal crystallization was performed as follows. First, the samples were heated to 200 °C for 5 min to erase the thermal history then quenched at a rate of 50 °C min^{-1}, reheated to the desired isothermal temperature (T_c = 110, 115, 120 and 125 °C) at a rate of 10 °C min^{-1} and held for 30 min to allow complete crystallization from the quiescent melt. The degree of crystallinity, X_c, was calculated using **Eq. 1**:

$$X_c(\%) = \frac{100.(\Delta H_m - \Delta H_{cc})}{\Delta H_m^0 . w_{PLLA}} \tag{1}$$

where ΔH_m and ΔH_{cc} are the melting enthalpies and the cold crystallization, respectively, ΔH_m^0 is the theoretical melting enthalpy of 100% crystalline PLLA (93.1 J g^{-1}) and w_{PLLA} is the weight fraction of PLLA in the composite.

For the Avrami analysis, the relative crystallinity conversion, χ_c, was calculated using **Eq. 2**:

$$\chi_c = \frac{\Delta H(t)}{\Delta H_{total}} \tag{2}$$

The isotherms were analyzed in Origin® using a special plugin developed by Lorenzo et al. for Avrami and Lauritzen-Hoffman studies [26]. The mass fraction of crystalline material, w_c, is proportional to χ_c. The volume fraction of converted material (V_c) is computed using **Eq. 3**, where the densities of amorphous and crystalline PLLA are assumed to be ρ_a = 1.25 g cm^{-3} and ρ_c =1.359 g cm^{-3}, respectively. Avrami plots were then obtained using **Eq. 5**.

$$V_c = \frac{W_c}{Wc + \left(\frac{\rho_c}{\rho_a}\right).(1-W_c)} \tag{3}$$

$$1 - V_c(t) = e^{(-kt^n)} \tag{4}$$

$$Log\left(-Ln\left(1 - V_c(t)\right)\right) = Log(k) + nLog(t) \tag{5}$$

The crystallization half-time ($t_{1/2}$) was calculated using **Eq. 6**:

$$t_{1/2} = \left(\frac{ln2}{k}\right)^{1/n} \tag{6}$$

2.6. Scanning electron microscopy (SEM) of the nanocomposites

The morphology was assessed by SEM observation of transverse section of cryogenically-fractured films. The surface was coated with a 1 nm-thick layer of platinum and viewed in a Zeiss Gemini 500 field-emission scanning electron microscope running at 1 kV and equipped with an in-lens secondary electron detector.

2.7. Tensile properties

Tensile tests were performed at room temperature (25 °C and 34 % relative humidity) using an Instron testing machine featuring a load cell with a maximum capacity of 100 N. Five specimens (10 mm × 40 mm) of each sample with a thickness of about 150 μm were used and a cross-head speed of 5 mm min^{-1} was applied.

2.8. Rheological properties

The rheological behavior of PLLA-PEG nanocomposites was characterized at 190 °C using an ARES-G2 TA Rheometer with a plate-plate geometry (25-mm diameter and 1-mm gap). The storage modulus, loss modulus, and complex viscosity were all measured as a function of frequency within the 0.01–10 Hz. An amplitude sweep, in the 0.1–100% deformation range at 1 Hz, was used to identify the linear viscoelastic region prior to each measurement.

2.9. Contact angle measurement

Thin NP films were prepared by casting 0.5 wt% suspensions in a Petri dish and drying at 40 °C for two days until complete evaporation of water. Contact angle measurements were carried out by depositing calibrated liquid drops on the surface of the films using an OCA 15 Drop Shape Analyzer from Dataphysics, equipped with a high-resolution CCD camera, working at an acquisition of 50 images per second. The data were analyzed with the OCA software. From the contact angles with water, glycerol and diiodomethane, the characteristics of the surface energy were determined using the Owens–Wendt equation (**Eq. 7**) [27]:

$$\frac{\gamma_L(1+cos\theta)}{2\sqrt{\gamma_l^d}} = \sqrt{\gamma_s^d} + \sqrt{\gamma_s^d} \times \sqrt{\frac{\gamma_L^P}{\gamma_L^D}} \tag{7}$$

$$\gamma_s = \gamma_s^p + \gamma_s^d \qquad\qquad (8)$$

where γ_x , γ_x^D, γ_x^P were the surface energy, the polar surface energy and the dispersive surface energy for each liquid probe ($x = l$) and the solid ($x = s$) NPs.

2.10. X-ray diffraction (XRD)

Strips of PLLA, PLLA-PEG and PLLA-PEG-NPs films before and after recrystallization were X-rayed under vacuum using a Philips PW3830 generator operating at 30 kV and 20 mA (Ni-filtered CuKα radiation, λ = 0.1542 nm). Two-dimensional diffraction patterns were recorded on Fujifilm imaging plates, read offline with a Fujifilm BAS 1800-II bioimaging analyzer. Profiles were calculated by rotational averaging of the 2D patterns.

3. Results and Discussion

The effect of the inclusion of the biobased nanofillers on the crystallization of the PLLA matrix was investigated by DSC under non-isothermal conditions by heating from the glassy state and cooling from the melt and under isothermal condition at different temperatures. To reduce the risk of aggregation of the nanofiller after water removal and facilitate their dispersion within the PLLA matrix via melt processing without any use of organic solvent, the aqueous suspension of the nanofiller was first mixed with PEG (the PEG content was kept constant at 5 wt% based on the PLLA weight) and then dried to remove water.

3.1 Morphology of the different biobased NPs

The shape and size of the different nanofillers differ according to their botanical origin and preparation route. Their average dimensions are given in **Table 2**. LCNFs (**Figs. 1A** and **S1A1**) and CNFs (**Figs. 1B** and **S1B1**) are very similar slender nanofibrils. Although it is difficult to measure their length with precision (about a few micrometers), higher magnification images show that they are often twisting bundles of a few elementary nanofibrils (**Fig. S1A2** and **S1B2**). Assuming a cylindrical cross-section, the diameter varies from 2 nm for individual nanofibrils to 6-8 nm for bundles.

CNCs (**Figs. 1C** and **S1C1**) and ChNCs (**Figs. 1D** and **S1D1**) are polydisperse spindle-like objects composed of a few laterally associated elementary crystallites that were not separated during the preparation process (**Fig. S1C2** and **S1D2**). Consequently, they can be described as irregular platelets [28]. However, the difference in average dimensions is marked. The length of ChNCs typically ranges between 150 to 1500 nm and the width between 10 and 60 nm, for average length and width of about 530 and 41 nm, respectively (**Table 2**). Their thickness can be estimated to 3-5 nm by measuring the width of the constituting unit crystallites (assuming a cylindrical

shape). The CNCs are shorter (50-250 nm) and narrower (2.5-20 nm), with an average length close to 200 nm. These dimensions are in reasonable agreement with those reported elsewhere for Celluforce CNCs [29]. Like for ChNCs, the thickness of CNCs would be close to that of an elementary crystallite, *i.e.* around 3 nm.
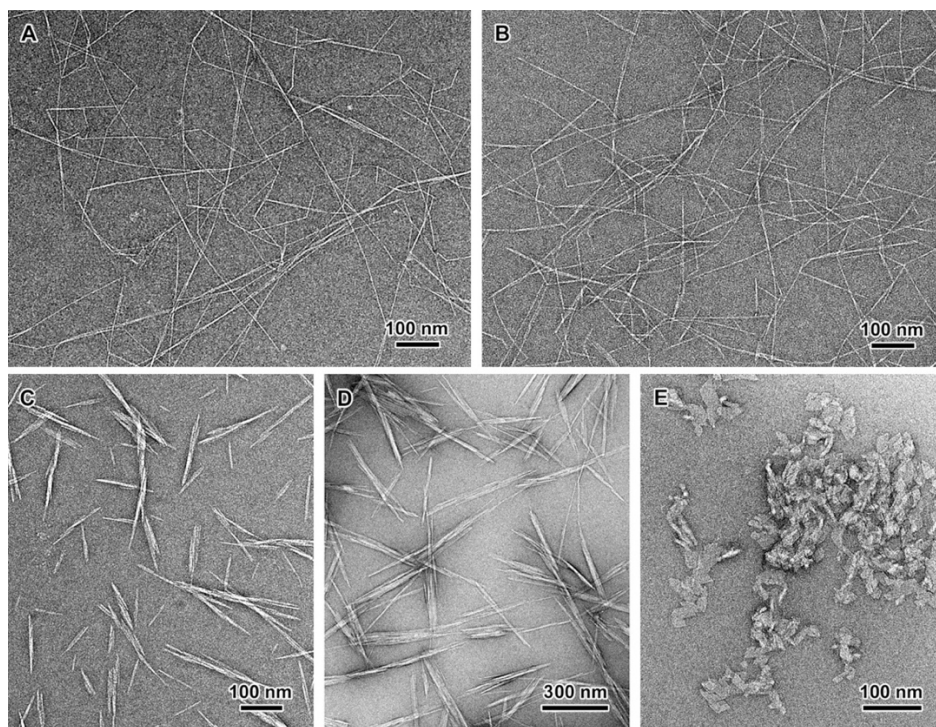

Figure 1. TEM images of negatively stained preparations of LCNFs (A), CNFs (B), CNCs (C), ChNCs (D) and SNCs (E).

SNCs are polydisperse polygonal platelets with an equivalent diameter ranging between 35 and 130 nm for individual particles (**Figs. 1E**, **S1E1** and **S1E2**). The platelet thickness (around 7 nm) is more regular and corresponds to that of the crystalline lamella separated by the acid-hydrolysis of native amylopectin [30]. However, since a partial aggregation is generally observed in the TEM preparations, likely due to drying and/or staining, the size of individual SNCs is difficult to evaluate and the hydrodynamic diameter determined by DLS from a SNC suspension appeared to be a more meaningful value, although it does not reflect the anisometry of the individual objects. The batch used in the present work was the same as the one characterized in our previous work [24]. The size distribution in a dilute SNC suspension was monomodal and centered at around 165 nm, with a polydispersity index of 0.11.

Table 2. Morphology and average dimensions of the NPs (std: standard deviation; n.d.: not determined).

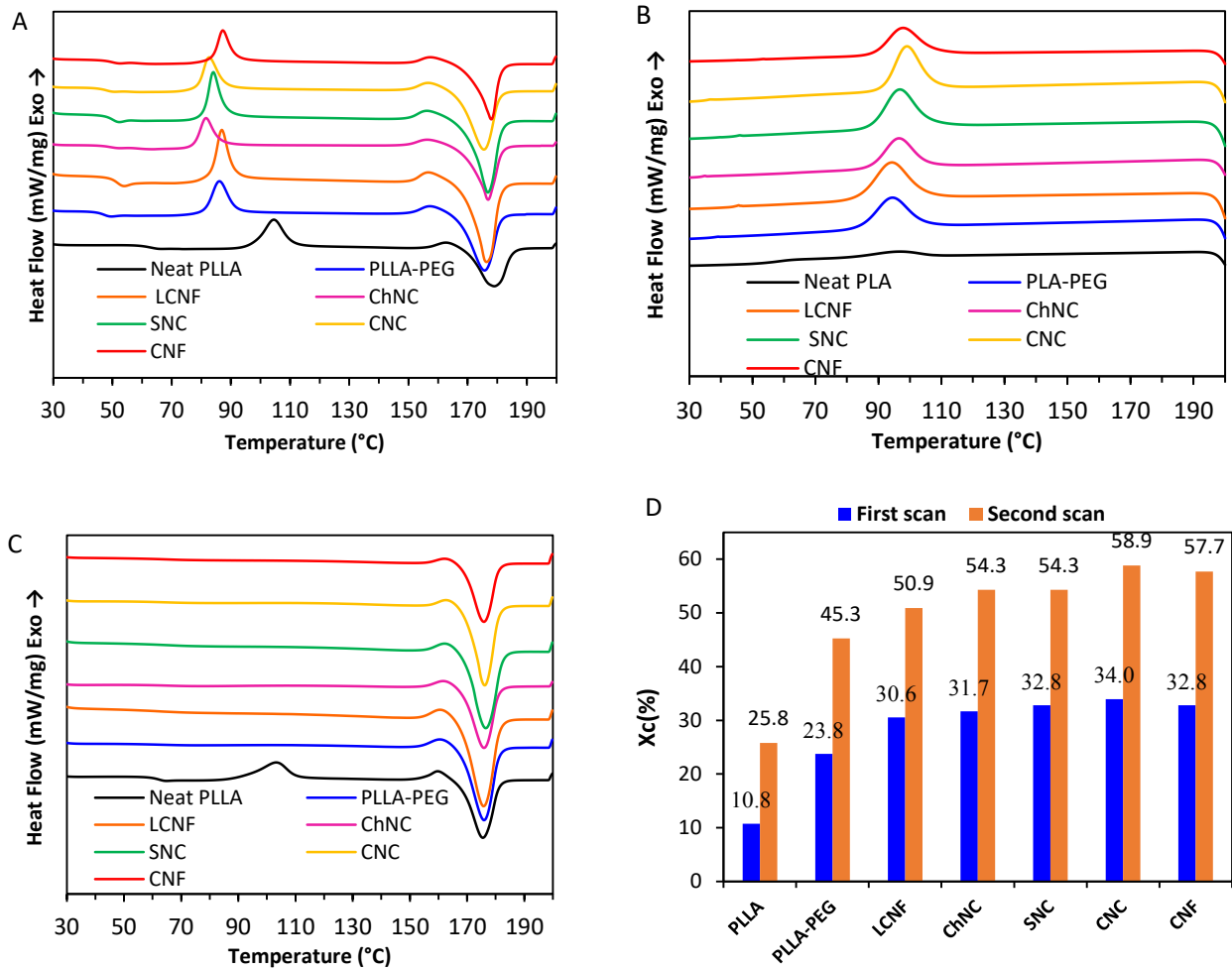| Nanoparticle	Length L [std] (nm)	Diameter / width D [std] (nm)	Thickness h [std] (nm)
LCNFs	n.d.	2 [0.5]	2 [0.5]
CNFs	n.d.	2 [0.5]	2 [0.5]
ChNCs	530 [277]	41 [16]	4 [0.5]
CNCs	188 [86]	13 [7]	3 [0.5]

Figure 2. (A) First DSC heating scans, (B) cooling plot, (C) second DSC heating scans, and (D) degree of crystallinity (X_c) after the first and second scans of PLLA, PLLA-PEG, and PLLA-PEG containing 1 wt% of the different NPs.

3.2. Non-isothermal crystallization kinetics

The DSC thermograms of PLLA containing 5 wt% PEG and in the presence of 1 wt% LCNFs, CNFs, CNCs, ChNCs, and SNCs, are shown in **Fig. 2**. After the first scan, all films show a cold

crystallization peak at a temperature between 105 and 80 °C, depending on the composition, followed by melting peak between 179 and 175 °C (**Fig. 2A**). Upon cooling, a crystallization peak between 95 and 100 °C was observed for all compositions (**Fig. 2B**), except for neat PLLA. On the second scan, only a melting peak was observed except for neat PLLA where the cold crystallization peak persisted, indicating that all samples crystallized during the cooling process (**Fig. 2C**). **Table S1** collects the different thermal property data extracted from DSC thermograms, including glass transition temperature (T_g), crystallization peak temperature (T_c), cold crystallization peak temperature (T_{cc}), melting peak temperatures (T_m), enthalpy of crystallization (ΔH_c), enthalpy of cold crystallization (ΔH_{cc}), enthalpy of melting (ΔH_m) and degree of crystallinity (X_c) recorded from the first and second scan. The neat PLLA without plasticizer has the lowest X_c (about 10 and 18%, after the first and second scans, respectively), confirming the poor tendency of PLLA to crystallization. The addition of 5% PEG plasticizer led to an increase in X_c, reaching 23 and 45% after the first and second scan, respectively, which indicates that PEG promoted the crystallization, presumably by facilitating the chain mobility of PLLA, as attested by the decrease in T_g. This result disagrees with that reported by Clarkson et al. [31] who pointed out an enhancement in the crystallization of PLLA only at 10 wt% PEG content. One reason for this discrepancy would be the difference in the molecular weight of the PEG used in both studies ($M_n = 35000$ g mol^{-1} in the present work against 600 in the cited paper).

The inclusion of the nanofiller markedly increased the crystallinity degree of PLLA, mainly after the second scan (**Fig. 2D**), with the highest effect observed for CNCs, ChNCs and CNFs bringing X_c in the 54-59% range. The lowest effect was observed in the presence of LCNFs with a X_c around 51%. A shift to a higher T_c by about 2 to 6 °C, with respect to PLLA-PEG, was also observed with the addition of the nanofiller with the highest magnitude noted for CNCs and CNFs (+6 °C), and the lowest for LCNFs and ChNCs. This indicates that the inclusion of the biobased NPs had a significant beneficial effect on the crystallization kinetics of PLLA during cooling by acting as a nucleating agent. However, their nucleating effect differs according to their origin.

Another remark worth pointing out is the shift to higher temperature of the T_g in PLLA-PEG when the nanofiller was added, where a T_g around 51-52 °C was noted for PLLA-PEG-NPs while its value was around 48.7 °C in the absence of nanofiller. A similar effect was noted for PLLA plasticized with triethyl-citrate in the presence of ChNCs [32]. One possible reason for the shift in T_g would be the difference in the crystallinity degree of the sample: more crystalline samples exhibit a higher T_g.
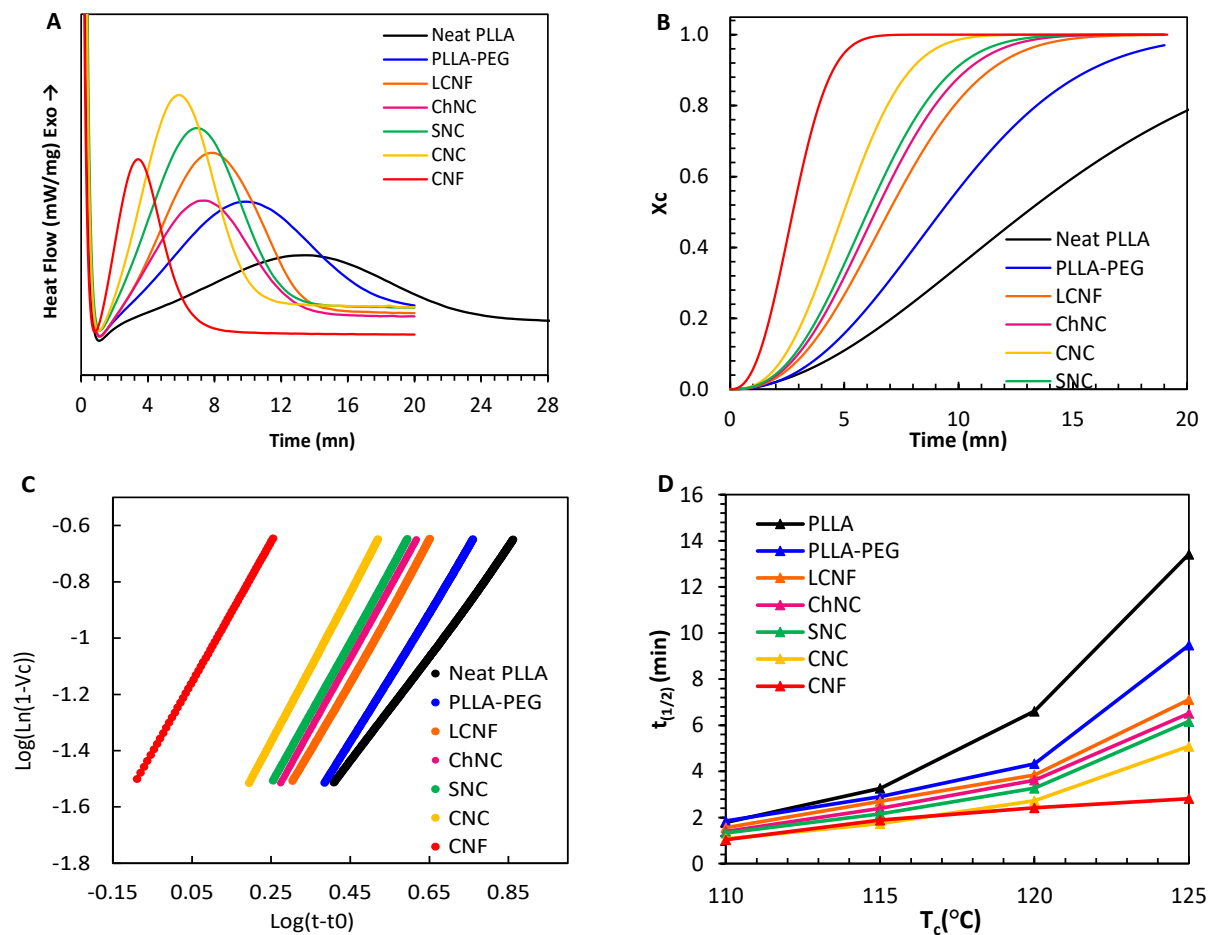
Figure 3. Avrami analysis from isothermal data at 125 °C: (A) Experimental isothermal data, (B) the relative crystallinity with time and (C) Avrami log-log plot, and (D) Half-time, $t_{1/2}$, versus T_c for PLA, PLLA-PEG, and PLLA-PEG containing 1 wt% of the different NPs.

3.3. Isothermal crystallization analysis

To further investigate the nucleating efficiency of the different biobased NPs, and try to understand how the structure and the morphology of the NPs are likely to affect the crystallization rate of PLLA, the isothermal melt crystallization kinetics was investigated using Avrami's formalism, from which the relative crystallinity degree $X(i)$ at time t was calculated from the specific heat flow, and Avrami's index n and rate constant k were extracted by using **Eq. 5**. At all tested temperatures, the relative crystallinity against crystallization time shows a typical sigmoid shape, as shown in **Fig. 3** reporting data at 125 °C for the different NPs, and in **Fig. S2** at 110 and 120 °C. The crystallization half-time ($t_{1/2}$), i.e. the time taken for 50% of the total crystallization to occur, is the simplest parameter to compare the nucleating efficiency of the different NPs. The reciprocal of $t_{1/2}$ measures the crystallization kinetics and is defined as the crystallization rate G. Accordingly, the shorter the halftime, the faster the crystallization rate, and vice versa. The kinetics data for the different NPs were collected in **Table S2**, from which the following remarks could be drawn:

12

- The neat PLLA has a slow crystallization, taking more than 30 min to achieve the crystallization at 125 °C, for example.

- The inclusion of 5 wt% PEG plasticizer decreased $t_{1/2}$, indicating that the addition of a small amount of plasticizer accelerated the crystallization kinetics, presumably by improving the chain mobility. This result agrees with literature data [33].

- All tested NPs have a beneficial effect on the crystallization kinetics of PLLA, with a markedly smaller $t_{1/2}$, mostly at a crystallization temperature (T_c) over 115 °C, with a magnitude which depends on the type of NPs. This indicates that the NPs are effective nucleating agents for PLLA. Based on the $t_{1/2}$ values, the order of nucleation efficiency is the following: CNFs ≈ CNCs > ChNCs > SNCs > LCNFs. For example, at 115 °C, it took about 15 and 10 min for neat PLLA and PLLA-PEG, respectively, to achieve crystallization, while this time decreased to about 8, 7, 6.5, 5.5, and 5 min in the presence of 1 wt% LCNFs, ChNCs, SNCs, CNCs and CNFs, respectively. The results concerning the effective nucleating efficiency of CNCs are in agreement with the work of Clarkson et al. [31].

- A strong dependence of the nucleation kinetics on the crystallization temperature is observed (**Fig. S3**), as attested by the steep decrease of $t_{1/2}$ with T_c, with a minimum around 110 °C. This result is expected and in line with the heterogeneous nucleation theory of polymers, because when T decreases, the driving force for crystallization, that is proportional to the difference between the equilibrium melting point and the crystallization temperature, increases with supercooling [34].

It is worth mentioning that most of the tested biobased NPs, namely CNFs, CNCs, ChNCs and SNCs are competitive in terms of nucleating efficiency with respect to other commercial nucleating agents reported in the literature [35,36].

The Lauritzen–Hoffman (L&H) nucleation theory [37], which quantitively correlates the crystallization growth rate with the temperature, was applied to further understand how the different NPs affected the crystallization of PLLA and explore their role on nucleation. According to the L&H theory, the linear growth rate (G) is given by **Eq. 9**:

$$G = G_0 \exp\left(\frac{-U^*}{R(T_c - T_\infty)}\right) \exp\left(\frac{-K_g}{T_c.\Delta T.f}\right) \qquad (9)$$

The linearized form is expressed by **Eq. 10**:

$$Ln\, G + \left(\frac{U^*}{R(T_c - T_\infty)}\right) = Ln\, G_0 - \frac{K_g}{T_c.\Delta T.f} \qquad (10)$$

where G_o is a pre-exponential factor, U^*, the activation energy required to bring the polymer chains to the crystallization site ($U^* = 1500$ cal mol^{-1}), K_g, the nucleation constant, R, the gas constant, and T_c, the crystallization temperature. T_∞ is the temperature at which diffusion ceases, which is

equivalent to T_g-30 °C, $\Delta T = T_m°$-T_c ($T_m°$ is the equilibrium melting temperature, was obtained using a nonlinear Hoffman-Weeks extrapolation [38]) and f is a correction factor given as $f = 2T_c / (T_c + T_m^0)$. K_g is the nucleation constant which reflects the energy needed for the formation of nuclei of critical size, and is defined by **Eq. 11**:

$$K_g = \frac{n.b.\sigma.\sigma_e.T_m^0}{\Delta H_m^0.K_b} \qquad (11)$$

where n is a constant equal 2 or 4 on the crystallization regimes [1], b, the layer thickness for PLLA (5.17 Å), σ the lateral surface free energy and σ_e are the fold surface free of the crystal/melt interfaces and ΔH_m^0 is the enthalpy of melting for 100% crystallinity $(\Delta H_m^0 = 1.26.10^8$ J.m$^{-3})$, and K_b, Boltzmann's constant $(1.38.10^{-23}$ J K$^{-1})$.

For all tested samples, the $Ln(G)+U^*/(R(T_c-T_\infty))$ *vs* $1/(T_c.\Delta T.f)$ (**Fig. 4**) gives a linear plot where the slope is $-K_g$ and the intercepts $\ln(G_0)$. The fold surface energy of the crystal/melt interfaces σ_e for the different NPs was also estimated using the Thomas–Stavely equation to calculate the lateral surface free energy, σ (**Eq. 12**):

$$\sigma = \alpha.\Delta H_m^0.(ab)^{1/2} \qquad (12)$$

where α is an empirical constant $(\alpha = 0.25)$, a is the molecular width (5.97 Å), b is the molecular layer thickness (5.17 Å) for PLLA, and $\Delta H_m^0 = 1.26.10^8$ J m^{-3} [21].

Table 3. Lauritzen–Hoffman parameters for PLLA-PEG and PLLA-PEG-NPs nanocomposites.

	T_m^0 (°C)	K_g (10^5 K^2)	σ_e (mJ m^{-2})	$\sigma.\sigma_e$ (10^4 J^2 m^{-4})	R^2
PLLA-PEG	197	5.95	81.20	12.50	0.9980
PLLA-PEG-LCNFs	188	4.41	61.30	9.44	0.9922
PLLA-PEG-ChNCs	183	3.69	51.90	7.99	0.9925
PLLA-PEG-SNCs	179	3.23	45.80	7.05	0.9953
PLLA-PEG-CNCs	176	2.90	41.30	6.36	0.9965
PLLA-PEG-CNFs	176	2.85	41.00	6.31	0.9949

From the data in **Table 3**, it can be seen that both K_g and σ_e values decreased with the incorporation of the different NPs, indicating a decreasing energy barrier of the nucleation process. This result is consistent with the analysis by Avrami. Another significant result from **Table 3** is the difference observed in σ_e according to the origin of the NPs, with the lowest value observed for CNFs, followed by CNCs, SNCs, ChNCs and finally LCNFs. The decrease in σ_e by the inclusion

of the NPs means that the chain folding of PLLA is easier in the presence of the NPs and the barrier energy for nucleation is thus lowered by the inclusion of the NPs than that for neat PLLA. Lower values of σ_e indicate a good nucleation efficiency since a lower amount of interfacial energy is required to form the crystal–substrate interface. The lower the σ_e, the faster the nucleation. It is worth mentioning that the product of the superficial energies of the crystals ($\sigma.\sigma_e$) for PLLA and PLLA-PEG is in good agreement with the value reported in the literature [39].
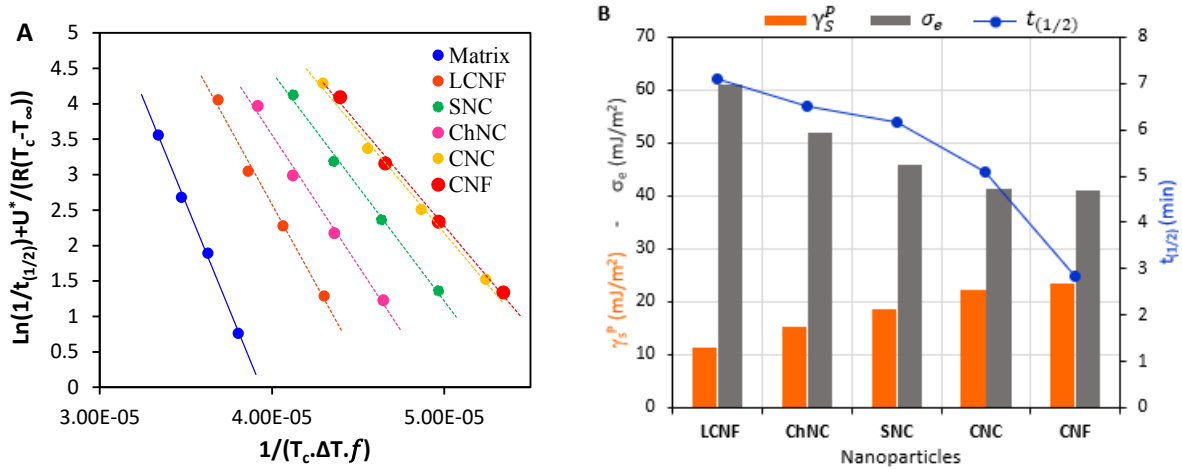

Figure 4. (A) Lauritzen–Hoffmann plots for PLLA-PEG (matrix) and the PLLA nanocomposites, and (B) γ_s^p, σ_e and $t_{1/2}$ at 125 °C relative to the different NPs.

Table 4. Contact angle, surface energy based on Owens–Wendt approach using three solvents: water, diiodomethane and glycerol.

Nucleating agent	Water (º)	Diiodomethane (º)	Glycerol (º)	γ_s^P (mJ m^{-2})	γ_s^D (mJ m^{-2})	γ_s (mJ m^{-2})
CNCs	43.1	32.4	19.3	22.0	31.4	53.4
CNFs	37.0	32.1	31.3	23.5	37.2	60.7
SNCs	43.1	34.0	43.4	18.5	34.8	53.3
ChNCs	55.4	32.3	30.7	15.2	35.4	50.6
LCNFs	68.0	38.4	70.0	11.4	37.2	48.6

Aiming at identifying a possible correlation between surface properties of the nanofiller and its nucleation efficiency, the dispersive and the polar components of to the surface energy of the different nanofiller were evaluated by contact angles measurement of three different liquids probes (water, glycerol, and diiodomethane), using the Owens–Wendt approach. In fact, referring to the L&H analysis, the nucleation ability of a nanofiller depends on its capacity to create a stable nucleus with a minimum lamellar thickness that will be stable at a given temperature.

Table 4 lists the calculated values of the dispersive (γ^D) and the polar (γ^P) components of the surface energy of the different NPs, and the corresponding linear plots was given in **Fig. S4**. The main difference observed between the different NPs lied on their γ^P, varying from 9 to 22 mJ m^{-2}, while γ^D did not significantly change, remaining at around 30 mJ m^{-2}. The highest value of γ^P was observed for CNFs and CNCs, followed by SNCs, ChNCs and LCNFs. This disparity is likely the result of a difference in surface functionalities among the different NPs. The high polar component in CNCs, SNCs and CNFs is presumably due to the presence of sulfate (SO_4^-) and carboxylic (COO^-) groups on the surface of CNCs/SNCs and CNFs, respectively. The presence of the sulfate groups ($-OSO_3^-$) at the surface of CNCs and SNCs results from the esterification reaction during sulfuric acid hydrolysis. In ChNCs, the lower value of may be explained by the presence of N-acetyl groups on the surface of ChNCs and the relatively low degree of deacetylation (DD) of the ChNCs (DD around 10%), meaning that about 90% of the N-acetyl groups were not hydrolyzed. The lowest magnitude of γ^P in LCNFs is due to the presence of residual lignin remaining attached to the surface of the LCNFs, imparting them a hydrophobic character, as attested by the water contact angle of 70°. Even if lignin is independent from the cellulose nanofibrils in LCNFs, the formation of CNC-lignin complexes with hydrogen bonds and hydrophobic interactions between lignin molecules and the surface of cellulose rods is likely to occur as demonstrated in the work of Hambardzumyan et al. [40].

Comparing the surface energy components of the different nucleating agents with $t_{1/2}$, it appears that the nanofiller with the highest γ^P has the lowest $t_{1/2}$ demonstrates the most effective nucleating aptitude (**Fig. 4B**). This is the case of CNCs and CNFs with γ^P of 22 and 23.5 mJ m^{-2} that display the highest nucleating efficiency for PLLA, while LCNFs with γ^P of 11.5 mJ m^{-2} and demonstrate the weakest effect. Crossing the results of surface energy components of the different NPs with the L&H analysis, where a decrease in the σ_e value was observed from LCNFs to ChNCs, SNCs, CNFs, and CNCs, we conclude that the increase in surface polarity of the NPs would contribute to enhance their nucleating efficiency for PLLA. The occurrence of specific PLLA−NPs interactions at molecular level might justify the difference in the nucleation kinetics between the different NPs. This interaction is driven by polar and hydrogen bonding between the surface of the NPs and the CO groups of PLLA, inducing a preferential orientation of PLLA chains on the surface of the NPs. This reorganization of PLLA chains facilitates the formation of a critical nucleus to overcome the energy cost for the chain-folding and creation of new surface. This led to a faster nucleation, with acceleration of the crystallization kinetics.

Even though most of the investigated NPs exhibited a fibrillar morphology, they differ by their aspect ratios, LCNFs and CNFs having the highest aspect-ratio, and CNCs and ChNCs the lowest ones. SNCs also differ by their platelet-like morphology, as confirmed from TEM observations

(**Fig. 1E**). From $t_{1/2}$ values and L&H analysis, it seems that the aspect-ratio is not the key parameter controlling the nucleating efficiency of the biobased NPs.

The XRD profiles of PLLA-PEG (prior and after annealing) and PLLA-PEG-NPs after annealing at 120 °C for 30 min are shown in **Fig. S5**. Considering the small amount of fillers, their contribution to the crystallinity cannot be detected in the profiles. Despite the presence of a melting peak in the DSC thermogram during the first scan, the XRD profile of the neat PLLA-PEG matrix is consistent with that of a poorly crystalline polymer. After annealing at 120 °C, the XRD profiles showed well-defined diffraction peaks. The five main peaks of the recrystallized PLLA-PEG matrix, located at $2\theta = 12.4, 14.7, 16.6, 18.9,$ and $22.2°$, can be assigned to the (004)/(103), (011), (200)/(110), (203)/(113), and (211) crystallographic planes of the orthorhombic α-allomorph, as expected at this crystallization temperature [41,42].

3.4. Rheological properties

Small-angle oscillation shear experiments were carried out to gain more insight on how the inclusion of NPs affects the processing behavior and viscoelastic properties of PLLA-PEG in the melt. Frequency sweep measurements of the storage (G') and loss modulus (G'') and the complex viscosity (η^*) at 190 °C were run under linear regime (**Figure 5A,B**). For the neat PLLA-PEG, the rheological behavior is typical of molten polymer with viscous character as attested by the much higher magnitude of G'' compared to G'. Storage modulus G'' being one magnitude higher than G' over the whole frequencies studied. A power-law relation over the frequencies domain with $G' \sim f^{1.7}$ and $G'' \sim f^{1}$, in the low frequency region, which is close to the theoretical exponent values of 2 for G' and 1 for G''. The deviation is likely due to the polydispersity of the commercial PLLA used. The complex viscosity, η^*, of PLLA-PEG exhibits a Newtonian plateau at low shear rates, with a slight shear-thinning behavior at a frequency of 5 Hz. PLLA-PEG under melt shows a purely viscoelastic behavior.

When the NPs were added to PLLA-PEG, η^*, G'' and G' increased, with an upward shift of the frequencies sweep plots with a magnitude that depended on the type of NPs (**Fig. 5A-D**). The strongest effect was observed for CNFs, followed by CNCs, SNCs, ChNCs and finally LCNFs that seem to induce the lowest effect on the melt-rheology of PLLA-PEG. For all tested NPs, the viscoelastic properties were still dominated by a liquid-like character with G'' exceeding about ten times G'. The power law slope of G' *vs.* f slightly decreased from 1.7 for PLLA-PEG to 1.55 and 1.6 in the presence of CNFs and CNCs, respectively. The increase in G' and the plateau of η^* nanofiller loading indicates a rigidification of the polymer melt, with increased resistance to flowing of polymer chains after inclusion of the NPs.
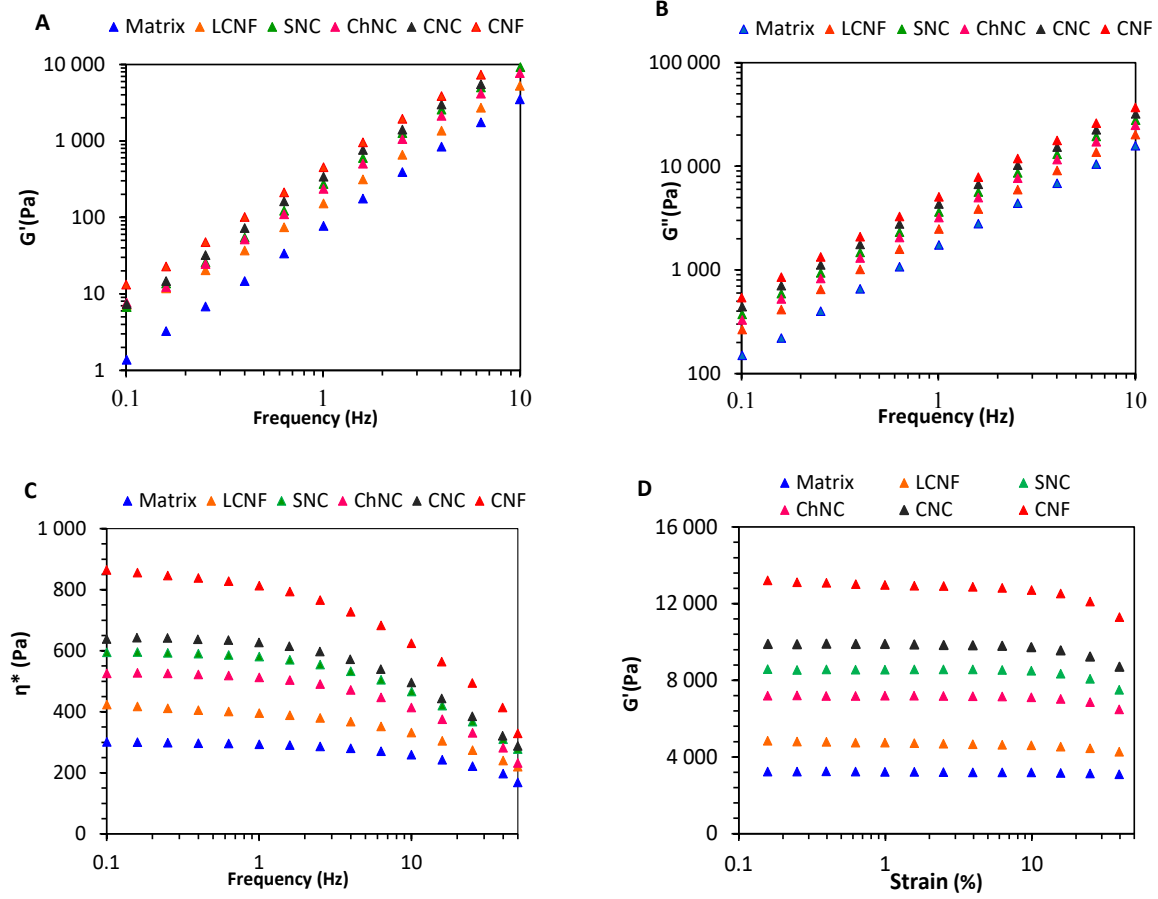
Figure 5. (A) Storage modulus (G'), (B) loss modulus (G''), (C) the complex viscosity (η^*) vs frequencies, and (D) storage modulus (G') *vs* strain at 1 Hz, at 190 °C of PLLA-PEG in the presence of NPs (Matrix: PLLA-PEG5%).

This effect may result from different contributions: (i) Brownian effect, (ii) hydrodynamic effects caused by the motion of solid NPs relative to the fluid medium, (iii) particle-particle interactions giving rise to a structured network, (iv) restriction of the mobility of polymer chains by the NPs as a result of specific interactions between the polymer matrix and the dispersed NPs.

The ratio of hydrodynamic forces to Brownian forces is defined by the Peclet number, Pe. For cylindrical particle in a medium of viscosity η_o, Kamal and Khoshkava [17] defined *Pe* as:

$$Pe = \frac{\pi \eta_o L^3 \dot{\gamma}}{3K_B T Ln\left(\left(\frac{L}{D}\right)-0.8\right)} \tag{13}$$

where K_B is Boltzmann's constant, T, the temperature and $\dot{\gamma}$, the shear rate. For viscoelastic fluid, the Cox–Merz [42] rule states that the steady-state viscosity η_o and complex viscosity η^* are equal when the shear rate $\dot{\gamma}$ is equal to pulsation $\omega = 2\pi f$. For $\eta_o = 300$ Pa s, and $w = 6.28$ s^{-1} ($f = 1$ Hz), *Pe* ranges from about 60 to 20,000 for the NPs. Pe is very high so hydrodynamic forces generated

by the added NPs are predominant, and account for the increment in η^*, G' and G'' of the PLLA-PEG-NPs under melting.

The particle-particle interactions may contribute to the rigidification of the molten polymer only over a critical threshold corresponding to the generation of a percolated network among NPs. However, the dominance of the viscous character of PLLA-PEG-NPs under melt ($G'' > G'$ over the whole frequencies studied) discards the possible build-up of a particle-particle network at 1 wt% nanofiller loading. Actually, for the biobased NPs studied, the set-up of a network inevitably led to an evolution of the viscoelastic character from a viscous to a solid-like material, G' being much higher than G''. Moreover, the rheological behavior does not show the appearance of a yield stress or a viscosity that tends to infinity at small frequencies typical of the existence of a percolation network of NP. Another confirmation of the lack of the set-up of a percolated network at 1 wt% comes from the estimation of the theoretical percolation threshold using (**Eq. 14**), which is widely used for a fibrillar morphology [43]:

$$\phi_p = \frac{0.7}{L/D} \qquad (14)$$

where L and D are the length and diameter of the particles. For a lamellar filler like SNCs, **Eq. 2** may still be used by replacing (L/D) with (D/h), where D and h are the diameter and thickness of the platelets, respectively.

L, D and h were evaluated from the TEM images (**Table 2**) and the corresponding ϕ_p estimated using **Eq. 14**. For CNCs, ChNCs and SNCs, we infer that 1 wt% of added nanofiller is unlikely to generate a percolated network in the PLLA-PEG matrix. Indeed, for these three types of NPs, the volume concentration ϕ_p is of the order of 7 % while the suspensions are concentrated to 0.6 % in volume. For NPs with high slenderness LCNFs and CNFs, ϕ_p is of the order of 0.3 %, (corresponding to about 0.6 wt%) thus lower than the concentration of the suspensions. This presumes the possibility of CNFs to form a percolated and entangled network. However, rheological data discard this hypothesis as the viscoelastic property of the PLLA-PEG-CNFs is dominated by a viscous character ($G'' > G'$ over the whole frequencies studied). The occurrence of a break-up of long CNFs along the weak point (kinks or amorphous regions) under the effect of a high-shear stress during melt-processing may be the origin of this divergence.

From the rheological analysis, it can also be pointed out that there is a marked difference in the melt-viscosity between LCNFs and CNFs while these two NPs have comparable morphologies. The lowest melt viscosity at low frequencies (**Fig. 5C**) was observed in the presence of LCNFs, followed by SNCs, ChNCs, CNCs and CNFs which had the highest viscosity. This means that the aspect ratio is not the main parameter controlling the melt-viscosity of PLLA-PEG-NPs.

The evolution of the critical strains between the linear to the non-linear regime under constant frequency also revealed differences according to the type of NPs (**Fig. 5C,D**). The strain under which the linear viscoelasticity (LVE) was conserved (at 95% of its original value) for PLLA-PEG and PLLA-PEG-LCNFs extended up to 60%, while the linear region was shorter in the presence of ChNCs, SNCs, CNCs and CNFs, with a deviation from linearity starting at 30 % deformation. The decrease in the magnitude of G′ and G″ over a critical strain is indicative of the occurrence of a microstructure break-down of the melt polymer. The origin of the microstructure might result from specific physical interaction between the polymer matrix and the dispersed NPs.

3.5. Morphology of the nanocomposite films before annealing

To examine the degree of dispersion of the NPs within the matrix, the cross-section of cryofractured films has been observed by SEM (**Fig. 6**). In the PLLA-PEG film, fibrils can be seen on the surface which presumably results from plastic deformation during fracture induced by the presence of the PEG plasticizer. In the films containing the NPs, the fractured surface showed tiny evenly dispersed particles. The size of the objects was less than 200 nm for LCNFs, CNFs, CNFs and ChNCs consistent with a good dispersion of the NPs within the PLLA matrix when PEG was used as a carrier. However, from these observations, it is difficult to confirm whether the particles were individualized or in the form of clusters. Even if partial aggregation among the NPs occurred, this aggregation is not excessive and the dispersed object remained at a nanoscale. It is important to mention that in the absence of PEG mediated dispersion agent, it was impossible to disperse the NPs within the PLA matrix by melt-processing. For SNCs, coarse particles can be seen, suggesting the occurrence of aggregation (**Fig. 6F2** and **6F3**).

3.6. Mechanical and optical properties

The evolution of the mechanical properties of the PLLA films after addition of the different nanofillers was studied by tensile test measurement, from which the elastic modulus (E), yield stress (σ_u), elongation at break (ε), and toughness were determined (**Table S3**). The stress−strain curves of the neat PLLA, PLLA-PEG, and PLLA-PEG-NPs are given in **Fig. 7**. The addition of 5 wt% PEG to PLLA resulted in a marked decrease in the ultimate stress and elastic modulus, by about 65 and 75%, respectively. This result agrees with the literature data [44] and is explained by the plasticizing effect of PEG that reduces the stiffness of the polymer and enhances the mobility of the polymer chains. In PLLA-PEG films containing the NPs, the evolution in the mechanical properties depended on their structure. An enhancement by about 50 to 100% in the tensile modulus and 20-30 % in ultimate stress (with respect to the PLLA-PEG matrix) was observed in the presence of SNCs, ChNCs, CNCs and CNFs while only moderate effect was noted in the presence of LCNFs.
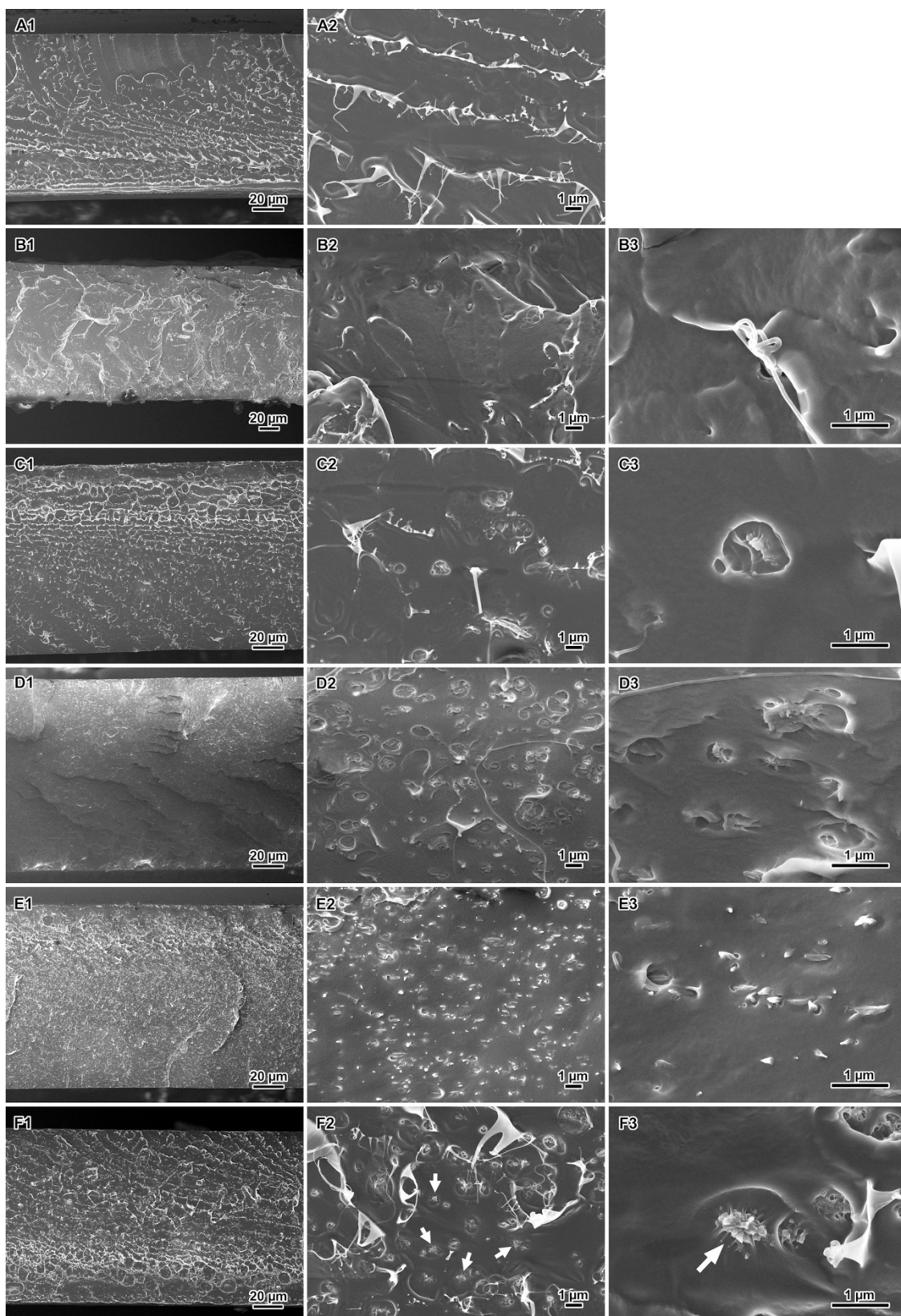
Figure 6. SEM images of cryofractured films of neat PLLA-PEG matrix (A1-2) and composite films incorporating 1 wt% LCNFs (B1-3), CNFs (C1-3), CNCs (D1-3), ChNCs (E1-3) and SNCs (F1-3). The arrows in F2 and F3 indicate possible SNC aggregates.
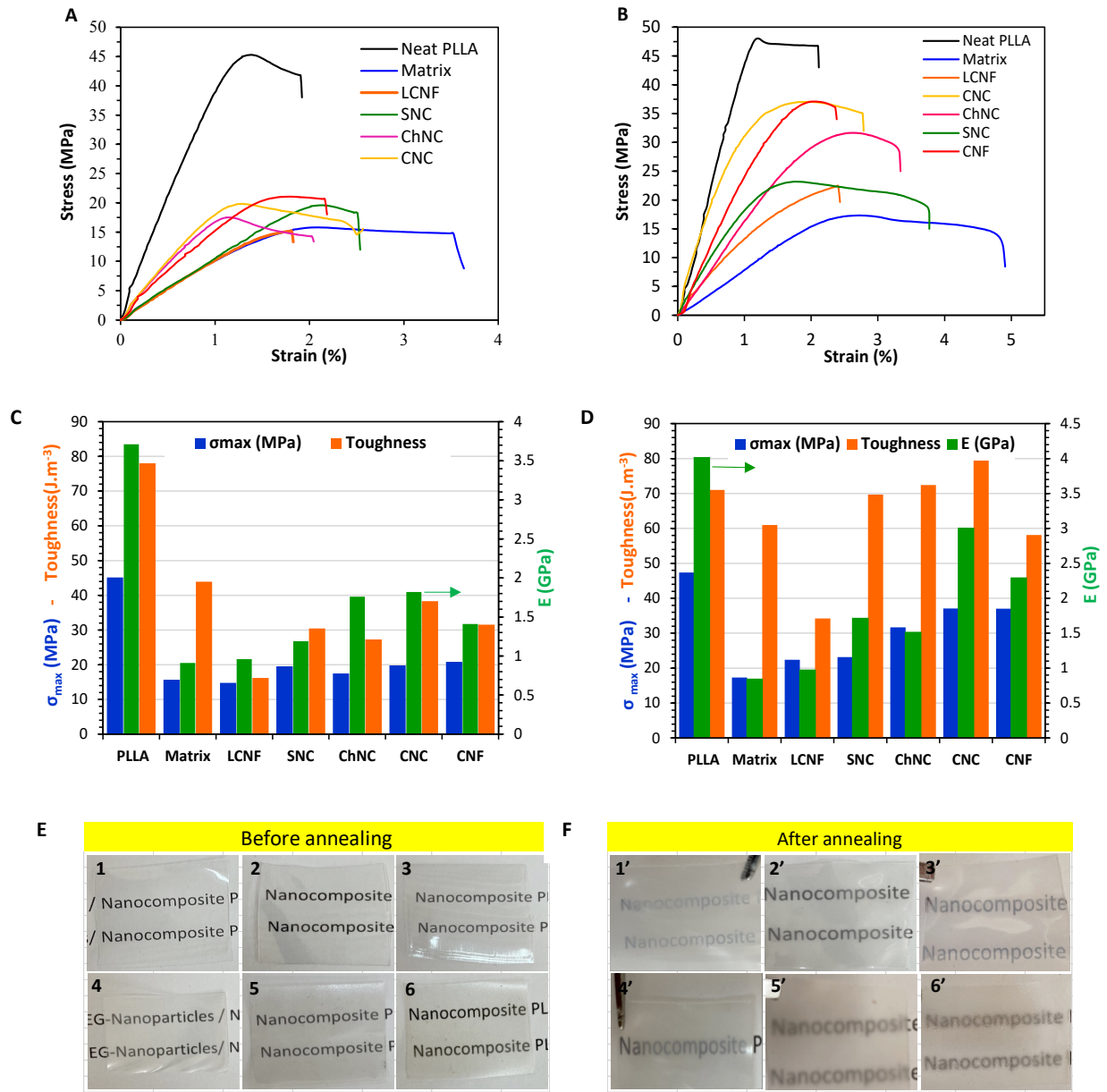
Figure 7. Stress-strain plots of neat PLLA and PLLA-PEG in the presence of the different NPs, (A) without, and (B) after annealing at 110 °C during 2 min. The corresponding maximum strength, toughness and E (C) without, and (D) after annealing. Photos of the films before(E) and after (F) the annealing treatment: Matrix (1 and 1´) CNCs (2 and 2´) ChNCs (3 and 3´) SNCs (4 and 4´) CNFs (5 and 5´) LCNFs (6 and 6´).

However, after an annealing treatment during 3 min at 110 °C, an obvious evolution in the tensile-stress plot was noted in films containing the NPs, while the evolution was minor in the PLLA-PEG matrix. Interestingly, it can be seen (**Fig. 7C,D**) that the enhancement in the tensile modulus and ultimate stress followed the same tendency as that noted for the nucleating efficiency, with the highest effect observed for CNCs, CNFs, followed by ChNCs, SNCs and LCNFs. It is also the same classification of the rheological properties of nanocomposites in the molten state. The increment in E/σ_u was about 400/115, 200/114, 78/80, 145/34, and 15/25 % for CNCs, CNFs, ChNCs, SNCs and LCNFs, respectively. The toughness of the material was also significantly enhanced in the presence of SNC and ChNC, reaching 82 and 72×10 J m^{-3}, respectively, which is higher than that of neat PLLA. This marked enhancement in the stiffness and strength is the consequence of the crystallization of PLLA, induced by the NPs to attain their maximum degree of crystallinity around 59%. The crystalline phase will act as a reinforcement for the matrix thanks to its high rigidity. The transparency degree of the films before and after annealing at 120 °C during 3 min depended on the origin of the NPs. Prior to annealing, the extruded films have a high transparency, with a transmittance ranging from 83 to 92 % (**Fig. S6**). The transmittance notably decreased after annealing by more than 40 %, indicating a decrease in the transparency of the film, as confirmed from the photos of the films (**Fig. 7F**). The enhancement in the crystallinity of the films following the annealing treatment would inevitably result in an increase in the size of crystallites, resulting in more scattering of light and accordingly a reduction in the transparency of the film.

Although the addition of PEG plasticizer inevitably resulted in a reduction in the tensile modulus and strength of PLLA, the inclusion of a small amount of biobased NPs such as CNCs, ChNCs or CNFs in PLLA-PEG matrix would contribute to meaningfully enhance the modulus and strength, after a short annealing treatment, by accelerating the crystallization of PLLA. With a tensile strength and toughness exceeding 25 MPa, and 70 J m^{-3}, respectively, the material has enough mechanical performance to consider its application in packaging, as replacement of polypropylene (PP) or high-density polyethylene (HDPE) based materials.

4. Conclusions

In this study, PLLA-PEG-NPs nanocomposites were prepared via melt-processing using PEG as a carrier to disperse the NPs in a PLLA matrix. According to DSC data, the addition of NPs had a considerable nucleating effect on PLLA, leading to enhanced crystallization rate and crystallinity degree (X_c in the 54-59 % range for CNCs, ChNCs, and CNFs and around 51% for LCNFs). The nucleation parameters for PLLA-PEG-NPs nanocomposites were assessed using the Avrami and L&H theories. It was found that the nucleation efficiency of the various NPs followed this order:

LCNFs < ChNCs < SNCs < CNCs < CNFs. This difference was explained by the evaluation of surface properties of the nanofiller. An increase in the surface polarity of the NPs would contribute to enhance their nucleating efficiency for PLLA. SEM observation indicated homogeneous distribution of the NPs, without confirmation if the NPs were fully individualized or partially aggregated. The inclusion of a small amount of biobased NPs such as CNCs, ChNCs or CNFs in PLLA-PEG matrix would contribute to significantly enhance the modulus and strength, after a short annealing treatment, by accelerating the nucleation of PLLA. The increment in E/σ_u was about 400/115, 200/114, 78/80, 145/34, and 15/25 % for CNCs, CNFs, ChNCs, SNCs and LCNFs, respectively. According to the results of this study, biobased nucleation agents appear to be valuable nucleating agents for PLLA and can help reaching optimal mechanical properties. Based on surface energy measurement, we have evidenced the existence of a correlation between the surface energy components of the different nucleating agents, namely γ^P and $t_{1/2}$: The nanofiller with the highest γ^P has the lowest $t_{1/2}$, which means a high effective nucleating aptitude. We justified this finding by assuming that the increase in surface polarity of the NPs would contribute to enhance their nucleating efficiency for PLLA. This work highlights the critical role of surface chemistry in controlling the heterogeneous nucleation kinetics of PLLA.
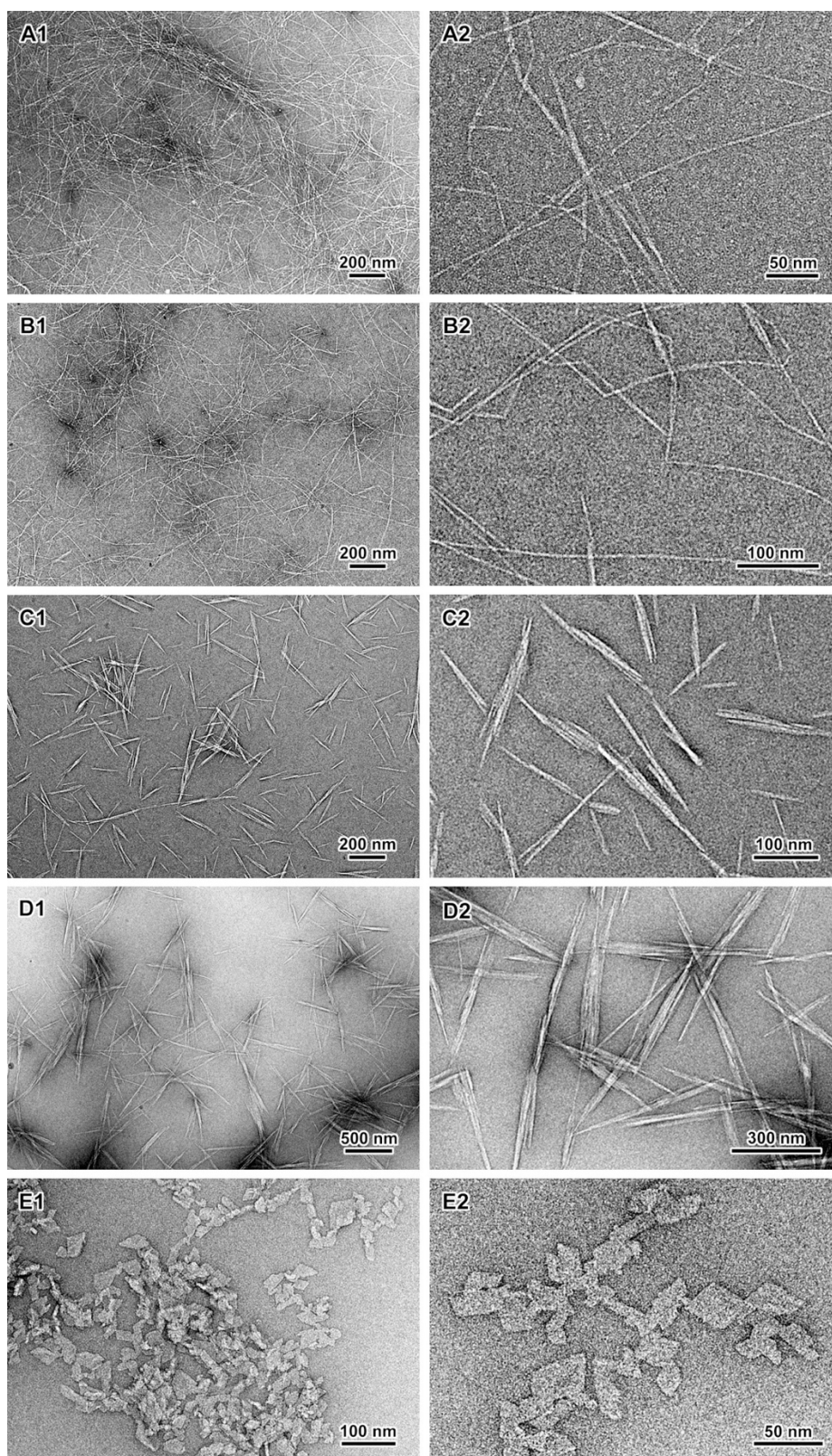
Figure S1. TEM images of negatively stained preparations of LCNFs (A1 and A2), CNFs (B1 and B2), CNCs (C1 and C2), ChNCs (D1 and D2) and SNCs (E1 and E2).
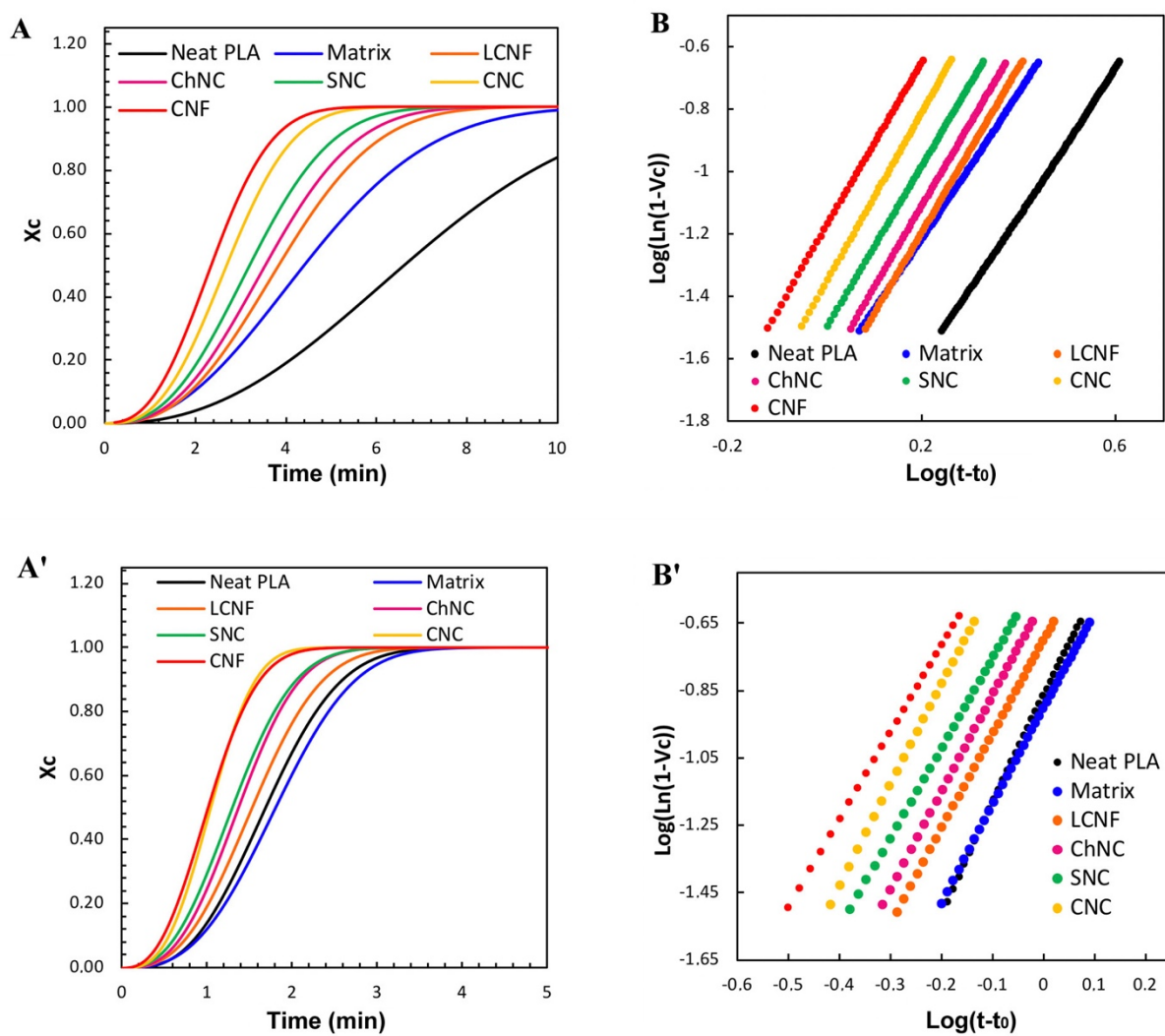
Figure S2: Progression of Avrami analysis from isothermal data: (A and A') Crystallinity conversion versus experiment time and (B and B') Avrami-type plot of Log(Ln(1-Vc)) *vs* Log(t-t$_0$) at 120 and 110 °C respectively.
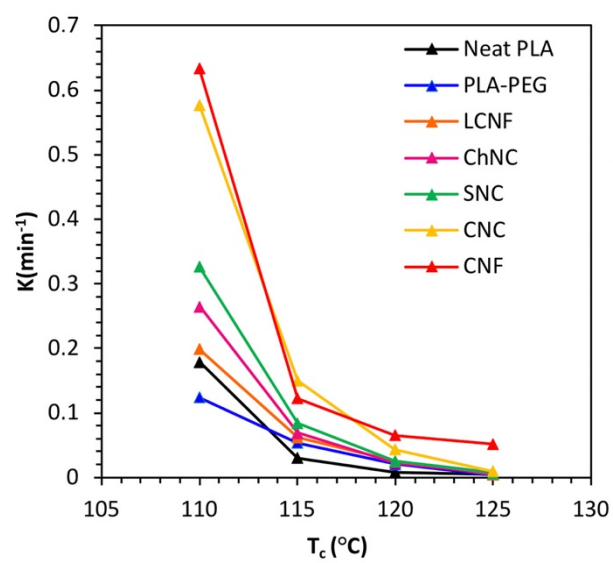
Figure S3: Crystallization rate K *vs* T_c for all compositions.

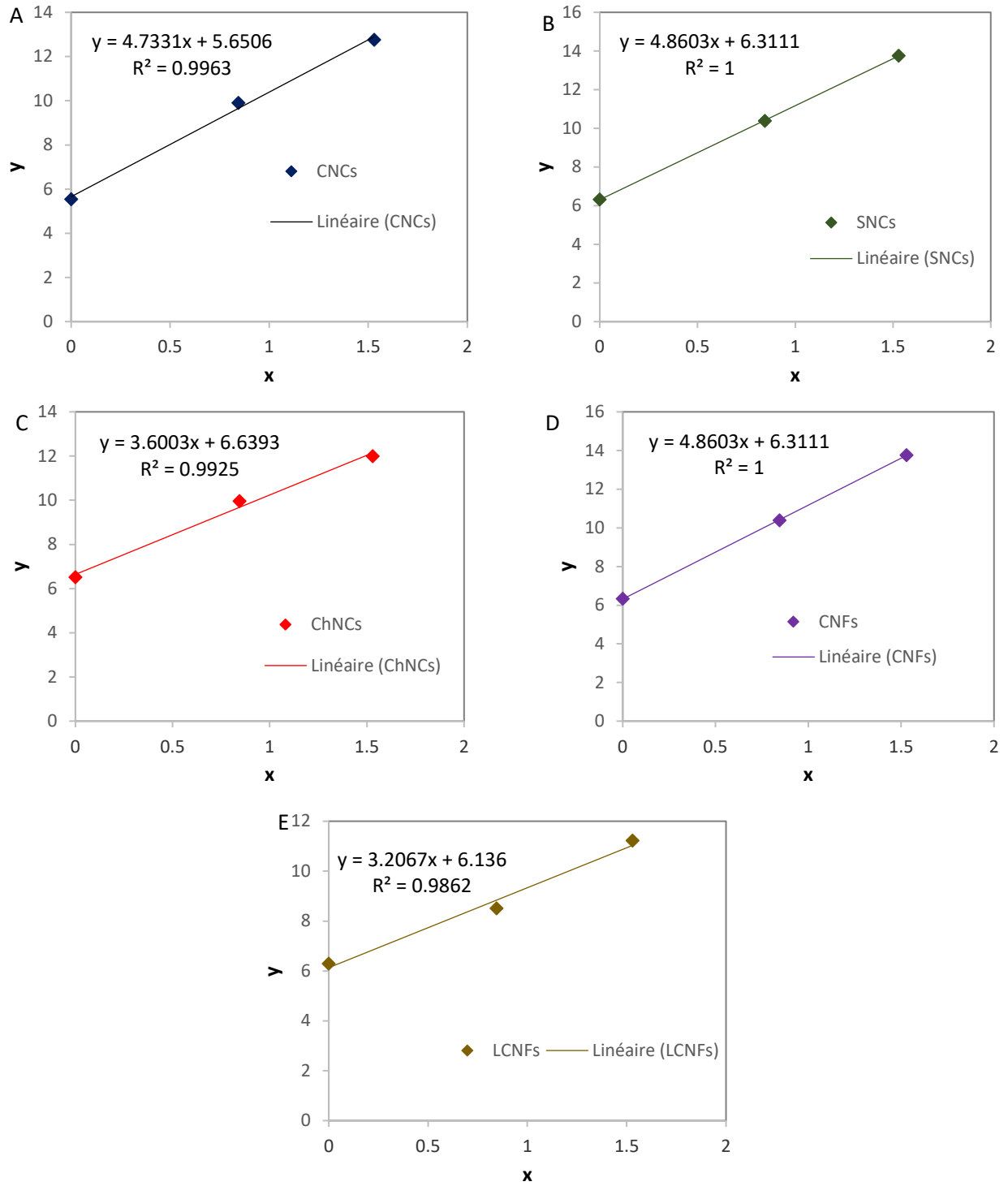**Figure S4**. Plot of $y = \sigma_l(\cos\theta + 1)/2 \left(\sqrt{\sigma_l^D}\right)$ as a function of $x = \sqrt{\sigma_l^P}/\sqrt{\sigma_l^D}$ for the different NPs: (A) CNCs, (B) SNCs, (C) ChNCs, (D) CNFs, and (E) LCNFs.
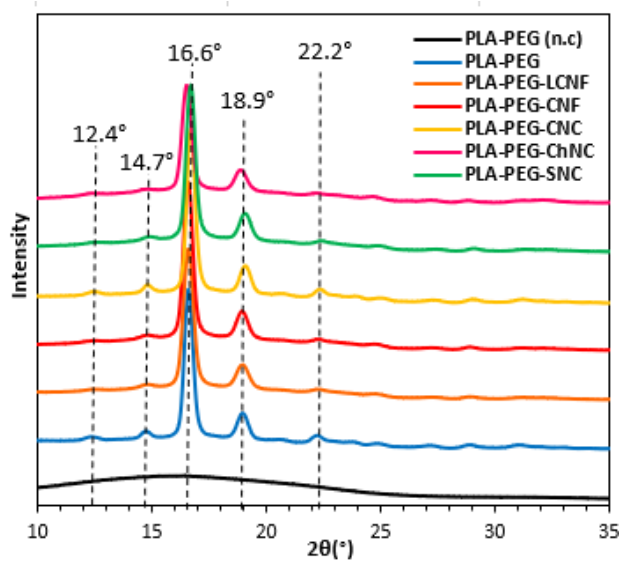
Figure S5: Comparison of the XRD profiles of non-crystallized PLA-PEG (n.c) and isothermally crystallized PLA–PEG, and PLA–PEG–NPS nanocomposites.
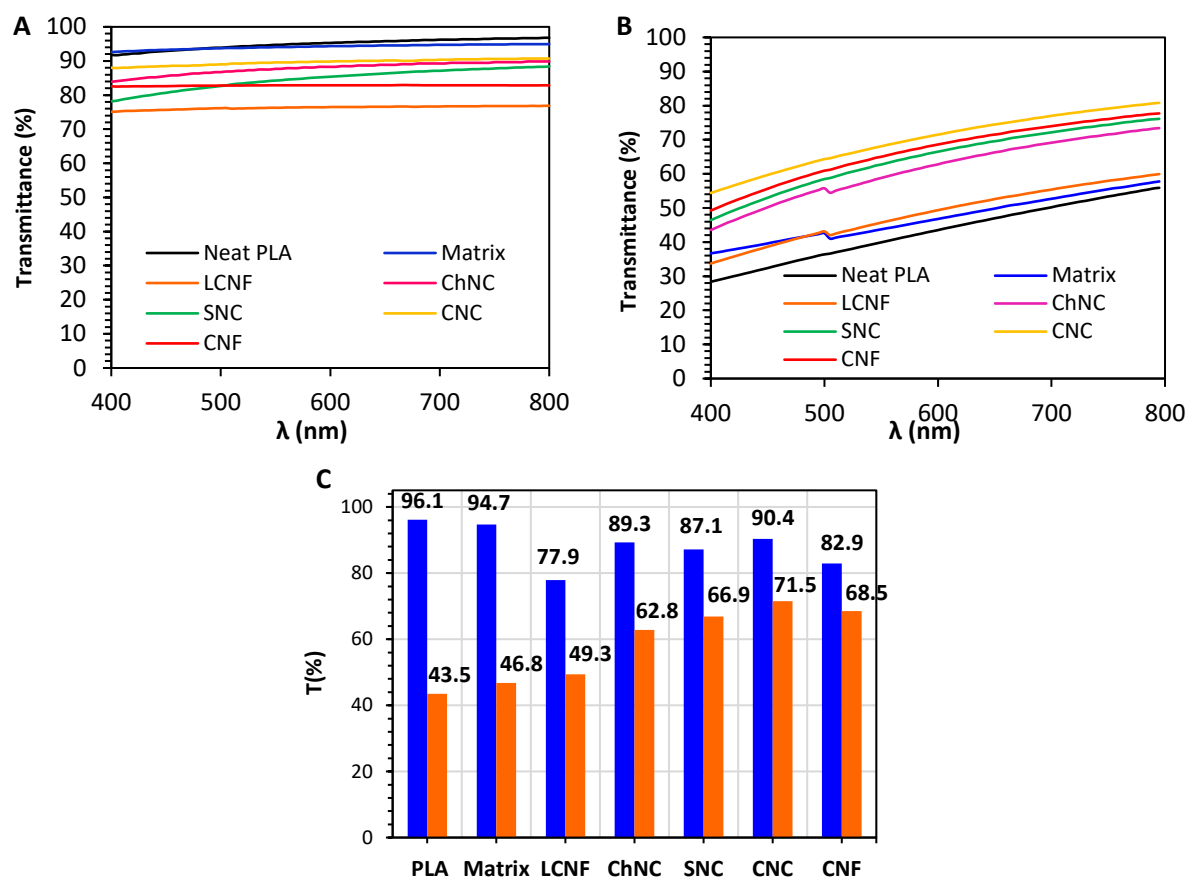
Figure S6: Transmittance of the extruded films before (A), and (B) after annealing at 120 °C for 3 min. (C) Transmittance at 600 nm before (blue) and after (orange) annealing at 120 °C.

Table S1. Thermal properties measured from non-isothermal experiments.

Sample	T_g (°C)	T_{cc}(°C)	T_c(°C)	T_m(°C)	ΔH_{cc} (J/g)	ΔH_m (J/g)	X_c (%)
Neat PLA	62.1	104.9	-	178.7	35	45	10.8
PLA-PEG	48.7	86.9	95.05	175.0	30	51	23.8
LCNF	52.2	87.0	94.94	175.2	34	61	30.6
ChNC	51.4	81.9	96.98	176.4	22	50	31.7
SNC	51.2	84.2	97.49	175.9	25	54	32.8
CNC	50.8	82.9	99.69	174.7	22	52	34.0
CNF	50.9	87.8	100.8	177.0	12	41	32.8

Table S2. Avrami parameters for isothermal crystallization of PLA-PEG-NPs nanocomposites.

	T_c (°C)	K (min^{-1})	n	$t_{1/2}$ (min)
Neat PLA	110	1.79 E-01	2.74	1.79
	115	3.03 E-02	2.64	3.27
	120	8.10 E-03	2.36	6.61
	125	5.05 E-03	1.90	13.40
PLA-PEG	110	1.24 E-01	2.87	1.85
	115	5.28 E-02	2.41	2.90
	120	2.05 E-02	2.33	4.33
	125	3.89 E-03	2.31	9.47
LCNF	110	1.98 E-01	2.80	1.54
	115	6.22 E-02	2.42	2.70
	120	2.50 E-02	2.46	3.85
	125	5.29 E-03	2.49	7.11
ChNC	110	2.65 E-01	2.87	1.39
	115	6.92 E-02	2.64	2.39
	120	2.27 E-02	2.66	3.62
	125	6.21 E-03	2.52	6.51
SNC	110	3.26 E-01	2.67	1.33
	115	8.34 E-02	2.75	2.16
	120	2.50 E-02	2.64	3.27
	125	7.00 E-03	2.53	6.10
CNC	110	5.76 E-01	2.98	1.08
	115	1.50 E-01	2.79	1.73
	120	4.27 E-02	2.76	2.73
	125	9.20 E-03	2.66	5.08
CNF	110	6.33 E-01	2.59	1.06
	115	1.22 E-02	2.73	1.89
	120	6.47 E-02	2.68	2.42
	125	5.21 E-02	2.49	2.82

Table S3. Ultimate strength, tensile modulus (E) and toughness before and after annealing treatment at 110 °C during 2 min.

	Before annealing			After annealing		
	σ_{max} (MPa)	E (GPa)	Toughness	σ_{max} (MPa)	E (GPa)	Toughness
Neat PLA	45.10	3.71	78.0	47.40	4.02	71.0
Matrix	15.69	0.91	43.9	17.31	0.85	61.0
LCNF	14.76	0.96	16.2	22.43	0.98	34.2
SNC	19.55	1.19	30.4	23.17	1.72	69.7
ChNC	17.47	1.76	27.3	31.65	1.52	72.4
CNC	19.82	1.82	38.3	37.05	3.01	82.0
CNF	20.81	1.41	31.5	37.03	2.30	58.1

References

[1] L.T. Lim, R. Auras, M. Rubino, Processing technologies for poly(lactic acid), *Prog. Polym. Sci.* 33 (2008) 820–852. https://doi.org/10.1016/J.PROGPOLYMSCI.2008.05.004.

[2] M. Drieskens, R. Peeters, J. Mullens, D. Franco, P.J. Iemstra, D.G. Hristova-Bogaerds, Structure versus properties relationship of poly(lactic acid). I. Effect of crystallinity on barrier properties, J. Polym. Sci. Part B Polym. Phys. 47 (2009) 2247–2258. https://doi.org/10.1002/POLB.21822.

[3] S. Saeidlou, M.A. Huneault, H. Li, C.B. Park, Poly(lactic acid) crystallization, *Prog. Polym. Sci.* 37 (2012) 1657–1677. https://doi.org/10.1016/J.PROGPOLYMSCI.2012.07.005.

[4] F. Yu, T. Liu, X. Zhao, X. Yu, A. Lu, J. Wang, Effects of talc on the mechanical and thermal properties of polylactide, *J. Appl. Polym. Sci.* 125 (2012) E99–E109. https://doi.org/10.1002/APP.36260.

[5] Z. Tang, C. Zhang, X. Liu, J. Zhu, The crystallization behavior and mechanical properties of polylactic acid in the presence of a crystal nucleating agent, *J. Appl. Polym. Sci.* 125 (2012) 1108–1115. https://doi.org/10.1002/APP.34799.

[6] S. Barrau, C. Vanmansart, M. Moreau, A. Addad, G. Stoclet, J.M. Lefebvre, R. Seguela, Crystallization behavior of carbon nanotube-polylactide nanocomposites, *Macromolecules* 44 (2011) 6496–6502. https://doi.org/10.1021/ma200842n.

[7] Z. Su, Q. Li, Y. Liu, G.H. Hu, C. Wu, Multiple melting behavior of poly(lactic acid) filled with modified carbon black, J. Polym. Sci. Part B Polym. Phys. 47 (2009) 1971–1980. https://doi.org/10.1002/POLB.21790.

[8] T. Xu, A. Zhang, Y. Zhao, Z. Han, L. Xue, Crystallization kinetics and morphology of biodegradable poly(lactic acid) with a hydrazide nucleating agent, *Polym. Test.* 45 (2015) 101–106. https://doi.org/10.1016/J.POLYMERTESTING.2015.05.009.

[9] R. Liao, B. Yang, W. Yu, C. Zhou, Isothermal cold crystallization kinetics of polylactide/nucleating agents, *J. Appl. Polym. Sci.* 104 (2007) 310–317. https://doi.org/10.1002/APP.25733.

[10] J.Z. Liang, L. Zhou, C.Y. Tang, C.P. Tsui, Crystalline properties of poly(L-lactic acid) composites filled with nanometer calcium carbonate, *Compos. Part B Eng.* 45 (2013) 1646–1650. https://doi.org/10.1016/J.COMPOSITESB.2012.09.086.

[11] B. Wang, T. Wen, X. Zhang, A. Tercjak, X. Dong, A.J. Müller, D. Wang, D. Cavallo, Nucleation of poly(lactide) on the surface of different fibers, *Macromolecules* 52 (2019) 6274–6284. https://doi.org/10.1021/acs.macromol.9B01078.

[12] Z. Wu, J. Lu, X. Wang, B. Hu, H. Ye, J. Fan, M. Abid, X. Zeng, Optimization for production of exopolysaccharides with antitumor activity in vitro from Paecilomyces hepiali, *Carbohydr. Polym.* 99 (2014) 226–234. https://doi.org/10.1016/j.carbopol2013.08.010.

[13] N. Zaldua, A. Mugica, M. Zubitur, A. Iturrospe, A. Arbe, G. Lo Re, J.M. Raquez, P. Dubois, A.J. Müller, The role of PLLA-g-montmorillonite nanohybrids in the acceleration of the crystallization rate of a commercial PLA, *CrystEngComm.* 18 (2016) 9334–9344. https://doi.org/10.1039/C6CE02005D.

[14] I.R. Mustapa, R.A. Shanks, I Kong, S. Chandran, Non-isothermal Crystallization of Poly(lactic acid)-hemp-silica nanocomposites plasticizes with tributyl citrate. Proc. Annual Condensed Matter and

Materials Meeting, Wagga Wagga, NSW (Australia), (2013) 33–36.
https://www.osti.gov/etdeweb/biblio/22719243

[15] F.A. dos Santos, G.C.V. Iulianelli, M.I.B. Tavares, Effect of microcrystalline and nanocrystals cellulose fillers in materials based on PLA matrix, *Polym. Test.* 61 (2017) 280–288. https://doi.org/10.1016/J.POLYMERTESTING.2017.05.028.

[16] K. Mondal, S. Sakurai, Y. Okahisa, V. V. Goud, V. Katiyar, Effect of cellulose nanocrystals derived from Dunaliella tertiolecta marine green algae residue on crystallization behaviour of poly(lactic acid), *Carbohydr. Polym.* 261 (2021) 117881. https://doi.org/10.1016/J.CARBPOL.2021.117881.

[17] M.R. Kamal, V. Khoshkava, Effect of cellulose nanocrystals (CNC) on rheological and mechanical properties and crystallization behavior of PLA/CNC nanocomposites, *Carbohydr. Polym.* 123 (2015) 105–114. https://doi.org/10.1016/J.CARBPOL.2015.01.012.

[18] E.M. Sullivan, R.J. Moon, K. Kalaitzidou, Processing and characterization of cellulose nanocrystals/polylactic acid nanocomposite films, *Materials* 8 (2015) 8106–8116. https://doi.org/10.3390/MA8125447.

[19] A. Pei, Q. Zhou, L.A. Berglund, Functionalized cellulose nanocrystals as biobased nucleation agents in poly(l-lactide) (PLLA) – Crystallization and mechanical property effects, *Compos. Sci. Technol.* 70 (2010) 815–821. https://doi.org/10.1016/J.COMPSCITECH.2010.01.018.

[20] P. Dhar, S.M. Bhasney, A. Kumar, V. Katiyar, Acid functionalized cellulose nanocrystals and its effect on mechanical, thermal, crystallization and surfaces properties of poly (lactic acid) bionanocomposites films: A comprehensive study, *Polymer* 101 (2016) 75–92. https://doi.org/10.1016/J.POLYMER.2016.08.028.

[21] A. Gupta, W. Simmons, G.T. Schueneman, E.A. Mintz, Lignin-coated cellulose nanocrystals as promising nucleating agent for poly(lactic acid), *J. Therm. Anal. Calorim.* 126 (2016) 1243–1251. https://doi.org/10.1007/S10973-016-5657-6.

[22] N. Herrera, A.M. Salaberria, A.P. Mathew, K. Oksman, Plasticized polylactic acid nanocomposite films with cellulose and chitin nanocrystals prepared using extrusion and compression molding with two cooling rates: Effects on mechanical, thermal and optical properties, *Compos. Part A Appl. Sci. Manuf.* 83 (2016) 89–97. https://doi.org/10.1016/J.COMPOSITESA.2015.05.024.

[23] F. Ben Cheikh, A. Ben Mabrouk, A. Magnin, J.-L. Putaux, S. Boufi, Chitin nanocrystals as Pickering stabilizer for O/W emulsions: Effect of the oil chemical structure on the emulsion properties, *Colloids Surf. B* 200 (2021) 111604. https://doi.org/10.1016/J.COLSURFB.2021.111604.

[24] E. Ben Ayed, A. Magnin, J.-L. Putaux, S. Boufi, Vinyltriethoxysilane-functionalized starch nanocrystals as Pickering stabilizer in emulsion polymerization of acrylic monomers. Application in nanocomposites and pressure-sensitive adhesives, *J. Colloid Interface Sci.* 578 (2020) 533–546. https://doi.org/10.1016/J.JCIS.2020.05.011.

[25] R. Baati, A. Ben Mabrouk, A. Magnin, S. Boufi, CNFs from twin screw extrusion and high pressure homogenization: A comparative study, *Carbohydr. Polym.* 195 (2018) 321–328. https://doi.org/10.1016/J.CARBPOL.2018.04.104.

[26] A.T. Lorenzo, M.L. Arnal, J. Albuerne, A.J. Müller, DSC isothermal polymer crystallization kinetics measurements and the use of the Avrami equation to fit the data: Guidelines to avoid common problems, *Polym. Test.* 26 (2007) 222–231. https://doi.org/10.1016/J.POLYMERTESTING.2006.10.005.

[27] D.K. Owens, R.C Wendt, Estimation of the surface free energu of polymers. *J. Appl. Polym. Sci.* 13 (1969) 1741-1747. https://doi.org/10.1002/app.1969.070130815

[28] E. Gicquel, J. Bras, C. Rey, J.-L. Putaux, F. Pignon, B. Jean, C. Martin, Impact of sonication on the rheological and colloidal properties of highly concentrated cellulose nanocrystal suspensions, *Cellulose* 26 (2019) 7619–7634. https://doi.org/10.1007/S10570-019-02622-7.

[29] M.S. Reid, M. Villalobos, E.D. Cranston, Benchmarking cellulose nanocrystals: From the laboratory to industrial production, *Langmuir* 33 (2017) 1583–1598. https://doi.org/10.1021/acs.langmuir.6B03765.

[30] H. Angellier-Coussy, J.-L. Putaux, S. Molina-Boisseau, A. Dufresne, E. Bertoft, S. Perez, The molecular structure of waxy maize starch nanocrystals, *Carbohydr. Res.* 344 (2009) 1558–1566. https://doi.org/10.1016/j.carres.2009.04.002.

[31] C.M. Clarkson, S.M. El Awad Azrak, G.T. Schueneman, J.F. Snyder, J.P. Youngblood, Crystallization kinetics and morphology of small concentrations of cellulose nanofibrils (CNFs) and cellulose nanocrystals (CNCs) melt-compounded into poly(lactic acid) (PLA) with plasticizer, *Polymer* 187 (2020) 122101. https://doi.org/10.1016/J.POLYMER.2019.122101.

[32] S. Singh, M.L. Maspoch, K. Oksman, Crystallization of triethyl-citrate-plasticized poly(lactic acid) induced by chitin nanocrystals, *J. Appl. Polym. Sci.* 136 (2019) 47936. https://doi.org/10.1002/APP.47936.

[33] Z. Kulinski, E. Piorkowska, Crystallization, structure and properties of plasticized poly(l-lactide), *Polymer* 46 (2005) 10290–10300. https://doi.org/10.1016/J.POLYMER.2005.07.101

[34] C. Schick, R. Androsch, Nucleation-controlled semicrystalline morphology of bulk polymers, *Polym. Cryst.* 1 (2018) e10036. https://doi.org/10.1002/PCR2.10036.

[35] V. Nagarajan, K. Zhang, M. Misra, A.K. Mohanty, Overcoming the fundamental challenges in improving the impact strength and crystallinity of PLA biocomposites: Influence of nucleating agent and mold temperature, *ACS Appl. Mater. Interfaces* 7 (2015) 11203–11214. https://doi.org/10.1021/ACSAMI.5B01145

[36] A. Shakoor, N.L. Thomas, Talc as a nucleating agent and reinforcing filler in poly(lactic acid) composites, *Polym. Eng. Sci.* 54 (2014) 64–70. https://doi.org/10.1002/PEN.23543.

[37] J.I. Lauritzen, Jr., J.D. Hoffman, Theory of Formation of Polymer Crystals with Folded Chains in Dilute Solution, *J. Res. Natl. Bur. Stand. Sect. A, Phys. Chem.* 64A (1960) 73. https://doi.org/10.6028/JRES.064A.007.

[38] J.J. Kolstad, Crystallization Kinetics of poly(L-lactide-co-meso-lactide). *J. Appl. Polym. Sci.* 62 (1996) 1079–1091. https://doi.org/10.1002/(SICI)1097-4628(19961114)62:7<1079::AID-APP14>3.0.CO;2-1

[39] R. Vasanthakumari, A.J. Pennings, Crystallization kinetics of poly(l-lactic acid), *Polymer* 24 (1983) 175–178. https://doi.org/10.1016/0032-3861(83)90129-5.

[40] A. Hambardzumyan, L. Foulon, B. Chabbert, V. Aguié-Béghin, Natural organic UV-absorbent coatings based on cellulose and lignin: Designed effects on spectroscopic properties, *Biomacromolecules* 13 (2012) 4081–4088. https://doi.org/10.1021/bm301373b.

[41] T. Kawai, N. Rahman, G. Matsuba, K. Nishida, T. Kanaya, M. Nakano, H. Okamoto, J. Kawada, A. Usuki, N. Honma, K. Nakajima, M. Matsuda, Crystallization and melting behavior of poly (L-lactic acid), *Macromolecules* 40 (2007) 9463–9469. https://doi.org/10.1021/ma070082c.

[42] W.P. Cox, E.H. Merz, Correlation of dynamic and steady flow viscosities, *J. Polym. Sci.* 28 (1958) 619–622. https://doi.org/10.1002/POL.1958.1202811812.

[43] M.A.S. Azizi Samir, F. Alloin, A. Dufresne, Review of recent research into cellulosic whiskers, their properties and their application in nanocomposite field, *Biomacromolecules* 6 (2005) 612–626. https://doi.org/10.1021/BM0493685.

[44] B.W. Chieng, N.A. Ibrahim, W.M.Z.W. Yunus, M.Z. Hussein, Plasticized poly(lactic acid) with low molecular weight poly(ethylene glycol): Mechanical, thermal, and morphology properties, *J. Appl. Polym. Sci.* 130 (2013) 4576–4580. https://doi.org/10.1002/APP.39742.